

Testing the Physical Parameter Constraining Power of HCN and HNC with Neural Networks

ERICA BEHRENS  ¹, JEFFREY G. MANGUM  ², MATHILDE BOUVIER  ³, COSIMA EIBENSTEINER  ^{2,*} AND SERENA VITI  ^{3,4,5}

¹ Department of Astronomy, University of Virginia, P. O. Box 400325, 530 McCormick Road, Charlottesville, VA 22904-4325, USA

² National Radio Astronomy Observatory, 520 Edgemont Road, Charlottesville, VA 22903-2475, USA

³ Leiden Observatory, Leiden University, P.O. Box 9513, NL-2300 RA Leiden, The Netherlands

⁴ Argelander Institut für Astronomie der Universität Bonn, Auf dem Hügel 71, 53121 Bonn Germany

⁵ Department of Physics and Astronomy, University College London, Gower Street, London WC1E 6BT

(Accepted 6 January 2026)

Submitted to The Astrophysical Journal

ABSTRACT

We quantify the utility of HCN and HNC to characterize gas conditions in the nearby starburst galaxy NGC 253. We use measurements from the Atacama Large Millimeter/Submillimeter Array (ALMA) Large Program ALCHEMI: the ALMA Comprehensive High-resolution Molecular Inventory. Using different subsets of the eight total HCN and HNC transitions measured by ALCHEMI, we test the number and combinations of transitions necessary for constraining the temperature, H₂ volume and column densities, cosmic-ray ionization rate, and beam-filling factor in three representative regions within NGC 253. We use these combinations of HCN and HNC transitions to constrain chemical and radiative transfer models and infer the gas conditions using a Bayesian nested sampling algorithm combined with neural network models for increased efficiency. By comparing the shapes of the resulting posterior distributions, as well as the medians and uncertainties for each gas parameter, from each test case to what we obtain with the full set of eight transitions (the control), we quantify how well each test reproduces the control. We find that multiple transitions each of both molecules are required to obtain a median parameter value within a factor of 2 of the control with an uncertainty less than 2–3 times that of the control. We also find that transition combinations that feature a range of upper-state energies are most effective. We show that single transitions, such as HCN $J = 1 - 0$ or $3 - 2$, are among the worst-performing combinations and result in parameter values up to an order of magnitude different than the control.

1. INTRODUCTION

Emission from molecular gas serves as a powerful tool for characterizing the physical conditions of gas in star-forming regions. The varying conditions (e.g. gas density, temperature, etc.) under which different molecules can be excited yields the opportunity to use individual or combinations of molecules as tracers of specific gas conditions or environments. In particular, molecular gas is chemically and physically influenced by the feedback processes from recently-formed nearby stars (E. Schinnerer & A. K. Leroy 2024, and references therein), such as shocks and cosmic-ray ionization from supernovae and their remnants (W. T. Reach et al. 2019; S. Vaupré et al. 2014; T.-Y. Tu et al. 2025) and ultraviolet (UV)

ionization from young stars (J.-L. Xu et al. 2019; C. Hernández-Vera et al. 2023). Understanding the impact of feedback processes on molecular gas helps us evaluate how the current generation of stars influences the material that will form the next generation. Some feedback mechanisms can have global effects on their host galaxies that influence the galaxies’ abilities to form future stars (T. M. Heckman et al. 1990; M. D. Lehnert & T. M. Heckman 1996; D. Ceverino & A. Klypin 2009; P. F. Hopkins et al. 2012; O. Agertz et al. 2013). For instance, cosmic rays from supernova feedback have been shown to create large-scale pressure gradients that result in outflows, which eject star-forming material into the circumgalactic medium and thereby suppress the star-formation rate (N. Peschken et al. 2023). It is thus important to fully understand how to use molecular emission to infer gas conditions; like temperature, density, and cosmic-ray ionization rate (CRIR); in order to piece together the impact of star formation on galaxy evolution.

Corresponding author: Erica Behrens
 eb7he@virginia.edu

* Jansky Fellow of the National Radio Astronomy Observatory

HCN in particular has been a popular molecule of study in extragalactic astronomy and is commonly used in ratios with other molecules to characterize dense, star-forming gas. In a seminal work regarding HCN's utility to study star formation, [Y. Gao & P. M. Solomon \(2004\)](#) used the HCN(1 – 0)/CO ratio as a dense gas tracer in a large sample of infrared galaxies. They additionally define an HCN-to-dense-gas conversion factor of $\alpha_{\text{HCN}} = 10 \text{ M}_\odot \text{ pc}^{-2} (\text{K km s}^{-1})^{-1}$. Since many extragalactic sources only feature measurements of single transitions due to sensitivity issues, many similar studies have since been performed that also use only single transitions, or ratios of single transitions, of HCN with CO and other molecules to identify correlations with infrared luminosity (e.g. [S. García-Burillo et al. 2012](#); [A. Usero et al. 2015](#)), star-formation rate (e.g. [A. Onus et al. 2018](#); [L. Neumann et al. 2024](#)), and other global galaxy characteristics. However, more recent studies have begun to reveal that the relationship between HCN and these other quantities is not so straightforward.

[S. Patra et al. \(2025\)](#) studied the dense gas conversion factor using HCN and HCO^+ 1 – 0 and found that even within our own galaxy, this factor depends greatly on the environment's metallicity and location within the Galaxy. Other studies have examined HCN 3 – 2/1 – 0 ratio in nearby galaxies and found that single transitions are not always reliable dense gas mass indicators ([F. Li et al. 2020](#)) and that no ratio uniquely traces any single gas excitation parameter, like temperature or density ([A. García-Rodríguez et al. 2023](#)). [G. H. Jones et al. \(2023\)](#) studied the gas density traced by the HCN 1 – 0 transition, which is typically considered to be a dense gas tracer, and found that in magnetohydrodynamical simulations, HCN emission can be found even when the cloud density is lower than its supposed characteristic density of $3 \times 10^4 \text{ cm}^{-3}$ ([Y. Gao & P. M. Solomon 2004](#)). This result is expanded in [A. R. Bemis et al. \(2024\)](#), which examined the HCN(1 – 0)/CO(1 – 0) ratio and determined that it will not always trace gravitationally bound star-forming gas. [A. Hacar et al. \(2020\)](#) explored the relationship between HCN and HNC in Milky Way star-forming environments, suggesting that the HCN/HNC $J = 1 - 0$ intensity ratio can be used as a temperature probe. However, the use of these molecules as a temperature tracer is uncertain and has been found to be temperature independent for $T \gtrsim 50 \text{ K}$ ([E. Behrens et al. 2022](#)). While [A. Hacar et al. \(2020\)](#) did compare their measurements to chemical models, the majority of these studies do not consider the chemical pathways related to HCN and HNC and their impact on observed intensities. Given these circumstances, more work is needed to understand how HCN can characterize molecular gas in star-forming regions and how this species is affected chemically by star-formation feedback mechanisms.

Studying HCN and HNC in extragalactic environments is essential for understanding the characteristics

of dense molecular gas in a broader range of environments than is accessible within the Milky Way alone. An ideal target for an extragalactic study of HCN and HNC is the nearby ($d \sim 3.5 \pm 0.2 \text{ Mpc}$, [R. Rekola et al. 2005](#)) starburst galaxy NGC 253. This nuclear starburst is forming stars at a rate of only $\sim 5 \text{ M}_\odot \text{ yr}^{-1}$, but with about half of that star formation occurring in just the central kiloparsec ([A. K. Leroy et al. 2015](#)). The molecular diversity of NGC 253's Central Molecular Zone (CMZ) has recently been studied in detail as a result of the ALMA Large Program ALCHEMI, the ALMA Comprehensive High-resolution Extragalactic Molecular Inventory ([S. Martín et al. 2021](#)). This program surveyed the molecular emission from 84.2 – 373.2 GHz, and the resulting measurements have been the focus of a wide range of studies analyzing the physical and chemical characteristics of this starburst CMZ ([J. Holdship et al. 2021](#); [N. Harada et al. 2021](#); [P. K. Humire et al. 2022](#); [J. Holdship et al. 2022](#); [N. Harada et al. 2022](#); [E. Behrens et al. 2022](#); [D. Haasler et al. 2022](#); [K. Y. Huang et al. 2023](#); [N. Harada et al. 2024](#); [M. Bouvier et al. 2024](#); [K. Tanaka et al. 2024](#); [M. Bao et al. 2024](#); [E. Behrens et al. 2024](#); [J. Butterworth et al. 2024](#); [R. Kishikawa et al. 2024](#); [Y. Gong et al. 2025](#); [M. Bouvier et al. 2025](#)).

Of these studies, [E. Behrens et al. \(2022, 2024\)](#) used the first four rotational transitions each of HCN and HNC ($J = 1 - 0$, $2 - 1$, $3 - 2$, and $4 - 3$) to constrain the gas parameters in the NGC 253 CMZ and found that HCN and HNC could effectively characterize the gas volume density and cosmic-ray ionization rate (CRIR). These studies found high volume densities and CRIRs in the center of the CMZ ($n_{\text{H}_2} \sim 10^5 \text{ cm}^{-3}$, $\zeta \sim 3 \times 10^{-13} \text{ s}^{-1}$) that decreased towards the outskirts of the CMZ. [E. Behrens et al. \(2024\)](#) found that using multiple species and transitions of HCN and HNC to constrain chemical and radiative transfer models was necessary to accurately infer certain parameter values, particularly CRIR. However, very few galaxies feature a set of measurements as comprehensive as those from the ALCHEMI program, often making it difficult to robustly characterize the gas conditions with a high level of precision. Thus, it is not yet clear how many transitions of these frequently-observed molecules are necessary to infer the gas conditions in star-forming regions.

In this paper, we will test the ability and limits of different combinations of HCN and HNC transitions to constrain chemical and radiative transfer models and infer the gas conditions in starburst environments represented by NGC 253. We will examine what number and combination of transitions yield the best results for constraining various physical parameters to provide guidance to those seeking to use these molecules to characterize gas in star-forming regions. In Section 3, we will describe the Bayesian nested sampling algorithm we use to sample our gas parameter space and model observed intensities, as well as what regions within NGC 253 and

which combinations of transitions we will consider. We present the results of this analysis in Section 4, where we compare the results from each tested combination of HCN and HNC transitions to what can be obtained when using the full set available with ALCHEMI. In Section 5, we will discuss the implications of these results and provide guidance for choosing HCN and HNC transitions for constraining various gas parameters.

2. DATA

We will use the first four rotational transitions each of HCN and HNC ($J = 1 - 0, 2 - 1, 3 - 2$, and $4 - 3$), which were observed as part of the ALCHEMI Large Program during ALMA Cycles 5 (2017.1.00161.L) and 6 (2018.1.00162.S). These data feature a common resolution of $1''.6$ (~ 27 pc) and are sensitive to scales as large as 250 pc. Further details of the observations and measurements are described in S. Martín et al. (2021), and the details of the spectral line signal extraction and moment map generation can be found in E. Behrens et al. (2022, 2024). We have provided the integrated intensities and root-mean-square (RMS) values for all eight HCN and HNC transitions measured toward each of the three regions (see Section 3.3) we consider in this paper in Table 1. Of particular importance is our use of 3σ upper limits in place of measured intensities for some transitions in select regions that were not measured to have a signal-to-noise ratio (SNR) ≥ 3 . As discussed in E. Behrens et al. (2024), these limits are used so that our models are constrained by an equal number of HCN and HNC transitions in each region. The impacts of these limits on our results are discussed in Section 4 and 5.2.

3. BAYESIAN INFERENCE OF MOLECULAR GAS CONDITIONS

We explore the ability and limitations of HCN and HNC to estimate molecular gas properties by constraining chemical and radiative transfer models with different combinations of measured HCN and HNC transitions toward the NGC 253 CMZ. In the following, we describe the gas parameter space we explore, our Bayesian parameter sampling method, the regions within the CMZ we target, and the HCN and HNC transition combinations we test and molecular constraints for our models.

3.1. Bayesian Inference Model Review

Here we provide an overview of our modeling algorithm, which has been used previously and described in more detail in E. Behrens et al. (2022, 2024). We are interested in constraining the following gas parameters in the NGC 253 CMZ using HCN and HNC: kinetic temperature, T_K ; H_2 volume density, n_{H_2} ; cosmic-ray ionization rate (CRIR), ζ ; H_2 column density, N_{H_2} ; and a beam-filling factor, η_{ff} . E. Behrens et al. (2022) and E. Behrens et al. (2024) constrained the gas conditions in the NGC 253 CMZ using HCN and HNC and

found that gas densities and CRIRs featured a distribution where these parameters peaked in the center of the CMZ, where most of the sources related to recent star formation are located, and decreased toward the outskirts. These studies found that H_2 volume and column densities, as traced by HCN and HNC ranges from $\sim 3 \times 10^3 - 10^5 \text{ cm}^{-3}$ and $\sim 2 \times 10^{22} - 5 \times 10^{24} \text{ cm}^{-2}$, respectively. The CRIR ranges from $\sim 10^{-14} \text{ s}^{-1}$ to $\sim 4 \times 10^{-13} \text{ s}^{-1}$. E. Behrens et al. (2024) also noted that the beam-filling factor η_{ff} was lower in the center of the CMZ (~ 0.1) and higher near the outskirts (~ 0.5), indicating that HCN and HNC are emitting from smaller, denser components in the center of the CMZ while being more diffuse near the outskirts. Both studies were unable to constrain the kinetic temperature with HCN and HNC measurements, stating that the abundances of these two species were primarily influenced by cosmic-ray ionization, not mechanical heating, thus making it impossible to determine T_K in this environment using HCN and HNC.

As in these previous studies, we use a forward model that includes both chemical and radiative transfer modeling, and we compare the results of these models to the measured HCN and HNC integrated intensities described in Section 2. Our chemical modeling component is derived from the two-phase gas-grain chemical code UCLCHEM (J. Holdship et al. 2017), which produces molecular abundances of HCN and HNC given a set of values for T_K , n_{H_2} , ζ , and N_{H_2} . Note that cosmic-ray ionization is our primary excitation mechanism and that we do not consider UV ionization in this model. E. Behrens et al. (2024) demonstrated that cosmic-ray-versus UV-dominated regions can be identified by examining the HCN/HNC abundance ratios—when this abundance ratio is near unity, the chemistry of these two molecules is primarily influenced by cosmic rays, with little effect from UV radiation. Alternatively, if the HCN/HNC abundance ratios is greater than ~ 4 , HCN is being enhanced as a result of UV ionization. We have chosen to focus here on regions within NGC 253 (further described in Section 3.3) that are known to be cosmic-ray-dominated, and thus use a constant value of 1 Habing for the UV radiation field.

To improve the efficiency of our modeling algorithm, we have trained a neural network from the output of a grid of UCLCHEM models to replace the role of a chemical code in our algorithm. This neural network model (details of which can be found in E. Behrens et al. 2024) improves the speed of our algorithm by a factor of 10. After acquiring HCN and HNC abundance predictions from the neural network model, we convert these abundances to integrated intensities using the non-LTE radiative transfer model RADEX (F. F. S. van der Tak et al. 2007) via the Python wrapper SpectralRadex (J. Holdship et al. 2021). With RADEX, we employ the default spherical geometry and assume a standard ortho:para H_2 ratio of 3:1. We then multiply the output integrated

Table 1. Integrated intensity and RMS values for the regions studied in this work.

Transition	Rest Frequency	E_u	Low- $n\zeta$		High- $n\zeta$		Low-SNR	
			(GHz)	(K)	(K km s $^{-1}$)			
HCN	1 – 0	88.6316	4.25	286	43	533	80	51
	2 – 1	177.2611	12.76	202	31	509	76	63
	3 – 2	265.8864	25.52	94	14	379	57	5.6
	4 – 3	354.5055	42.53	42	6	261	39	1.3 ^a
HNC	1 – 0	90.6636	4.35	126	19	459	69	28
	2 – 1	181.3248	13.05	32	9	288	44	26
	3 – 2	271.9811	26.11	28	4	245	37	1.9 ^a
	4 – 3	362.6303	43.51	9	1	148	22	1.8 ^a

^a 3σ upper limit

Table 2. Prior Distributions and Inferred Parameter Values

	Parameter	Range	Distribution Type	Low- $n\zeta$	High- $n\zeta$	Low SNR
T_K	Temperature (K)	50–300	Linear	279_{-84}^{+50}	$179.47_{-81.57}^{+100.56}$	115_{-47}^{+81}
n_{H_2}	Volume Density (cm $^{-3}$)	10^3 – 10^7	Log	$4.1_{-0.4}^{+0.4} a$	$4.93_{-0.44}^{+0.37} a$	$3.9_{-0.5}^{+0.4} a$
ζ	Cosmic-ray Ionization Rate (s $^{-1}$)	10^{-17} – 10^{-10}	Log	$-13.8_{-0.4}^{+0.5} a$	$-12.64_{-0.48}^{+0.40} a$	$-13.6_{-0.5}^{+0.5} a$
N_{H_2}	H ₂ Column Density (cm $^{-2}$)	10^{22} – 10^{25}	Log	$23.1_{-0.3}^{+0.5} a$	$24.43_{-0.46}^{+0.38} a$	$22.7_{-0.4}^{+0.9} a$

^a Value is given in logspace

intensities by the beam-filling factor η_{ff} and compare the modeled integrated intensities F_t to our measured values F_d and their uncertainties σ_F for each transition i using the following likelihood equation:

$$P(\mathbf{F}_d | \boldsymbol{\theta}) = \exp \left(-\frac{1}{2} \sum_i \frac{(F_{d,i} - F_{t,i})^2}{\sigma_{F,i}^2} \right). \quad (1)$$

where θ represents the gas parameters.

A lower likelihood value implies that the set of input parameters produced integrated intensities more similar to our measurements. Note that we assume all measured transitions are emitting from the same gas component, and thus we derive an average set of gas parameters for the bulk gas traced by HCN and HNC for each studied region (J. Holdship et al. 2022; E. Behrens et al. 2022, 2024).

3.2. Parameter Space and Sampling Method

To sample our parameter space and infer the gas conditions traced by HCN and HNC, we use a Bayesian nested sampling algorithm to constrain the chemical and radiative transfer models described in Section 3.1. The main difference in this work is the use of a different nested sampling code, **Nautilus**⁶ (J. U. Lange 2023). **Nautilus** is an importance nested sampling-based algorithm that uses neural networks to explore and sample the parameter space with increased efficiency. Both standard and importance nested sampling algorithms use a “live set”, which consists of the current set of parameter combinations, or live points, with the highest likelihoods. As new combinations within the parameter space are sampled, points are added to the live set if their likelihoods are higher than the lowest likelihood in the live set, which will then subsequently be removed.

However, standard nested sampling algorithms, such as those used in J. Holdship et al. (2022); E. Behrens et al. (2022, 2024), are often inefficient when sampling the parameter space—sampling too few points can compromise the accuracy of the algorithm, so these algorithms often err on the side of sampling a great number of points, prioritizing accuracy over efficiency. As a result, many more sampled points are rejected from, rather than added to, the live set.

Nautilus overcomes this limitation by (a) using importance nested sampling techniques (F. Feroz et al. 2019) and (b) employing neural networks to apply more efficient bounds to the parameter space. Importance nested sampling allows the algorithm to use all previous likelihood calls, rather than just those in the live set, to determine which volume of the parameter space to sample next by associating a weight with each likelihood call. This fact, in combination with **Nautilus**’s use of neural networks to draw sampling bounds, results

in a higher percentage of sampled points being added to the live set and thus makes fewer likelihood evaluations necessary to fully sample the parameter space.

3.3. Region Selection

We consider three regions in the NGC 253 CMZ in which to test the constraining power of HCN and HNC in starburst environments. E. Behrens et al. (2024) divided the CMZ into 94 50-pc regions (Figure 1) in order to sample GMC-scale structures and successfully constrained the gas conditions in many of these regions using 8 transitions of HCN and HNC. They identified a clear distribution in the gas conditions across the CMZ, with the highest volume densities and cosmic-ray ionization rates inferred toward the center and decreasing outward. Since other ALCHEMI studies (e.g. J. Holdship et al. 2022; K. Y. Huang et al. 2023; K. Tanaka et al. 2024; M. Bouvier et al. 2024) have also found that the molecular gas properties vary spatially over the NGC 253 CMZ, we select three regions that are representative of three different environments. The inferred parameter values for these 3 regions as determined by E. Behrens et al. (2024) are shown in Table 2.

We select region 53 (see Figure 1), hereafter referred to as the “high- $n\zeta$ region”, as an example of a central region with a high volume density ($n_{\text{H}_2} \sim 10^5 \text{ cm}^{-3}$) and cosmic-ray ionization rate (CRIR, $\zeta \sim 10^{-12.6} \text{ s}^{-1}$). We choose region 26, hereafter referred to as the “low- $n\zeta$ region”, as an example of an environment farther from the nucleus with more moderate gas conditions ($n_{\text{H}_2} \sim 10^4 \text{ cm}^{-3}$, $\zeta \sim 10^{-13.8} \text{ s}^{-1}$). In both of these regions, we detected 4 transitions each of HCN and HNC with a signal-to-noise ratio (SNR) of at least 3. Though these regions are meant to distinctly represent more intense (high- $n\zeta$) and more moderate (low- $n\zeta$) conditions, they are neither the most extreme nor most quiescent regions within NGC 253. They have instead been chosen to signify represent environments that could be generalized to many sources in the nearby universe.

We also chose to study region 51, hereafter referred to as the “low-SNR region”, which is located near the outskirts of the CMZ. E. Behrens et al. (2024) detected only 5 total HCN and HNC transitions toward the low-SNR region with a $\text{SNR} \geq 3$: HCN $J = 1 - 0$, $2 - 1$, and $3 - 2$; and HNC $J = 1 - 0$ and $2 - 1$. We chose this region due to its incomplete transition set as well as the fact that it is not strongly affected by UV, unlike many other low-signal regions on the outskirt of NGC 253 (E. Behrens et al. 2024). Including the low-SNR region in our analysis will allow us to assess the impact of measurement SNRs on the constraining power of molecular transitions, while still employing the model framework described in Section 3.1. As per E. Behrens et al. (2024), we substitute 3σ limits for the transitions that were not detected with $\text{SNR} \geq 3$ to use an equal number of constraining measurements per region—as indicated in Equation 1, our log-likelihood function with

⁶ <https://nautilus-sampler.readthedocs.io/en/latest/index.html>

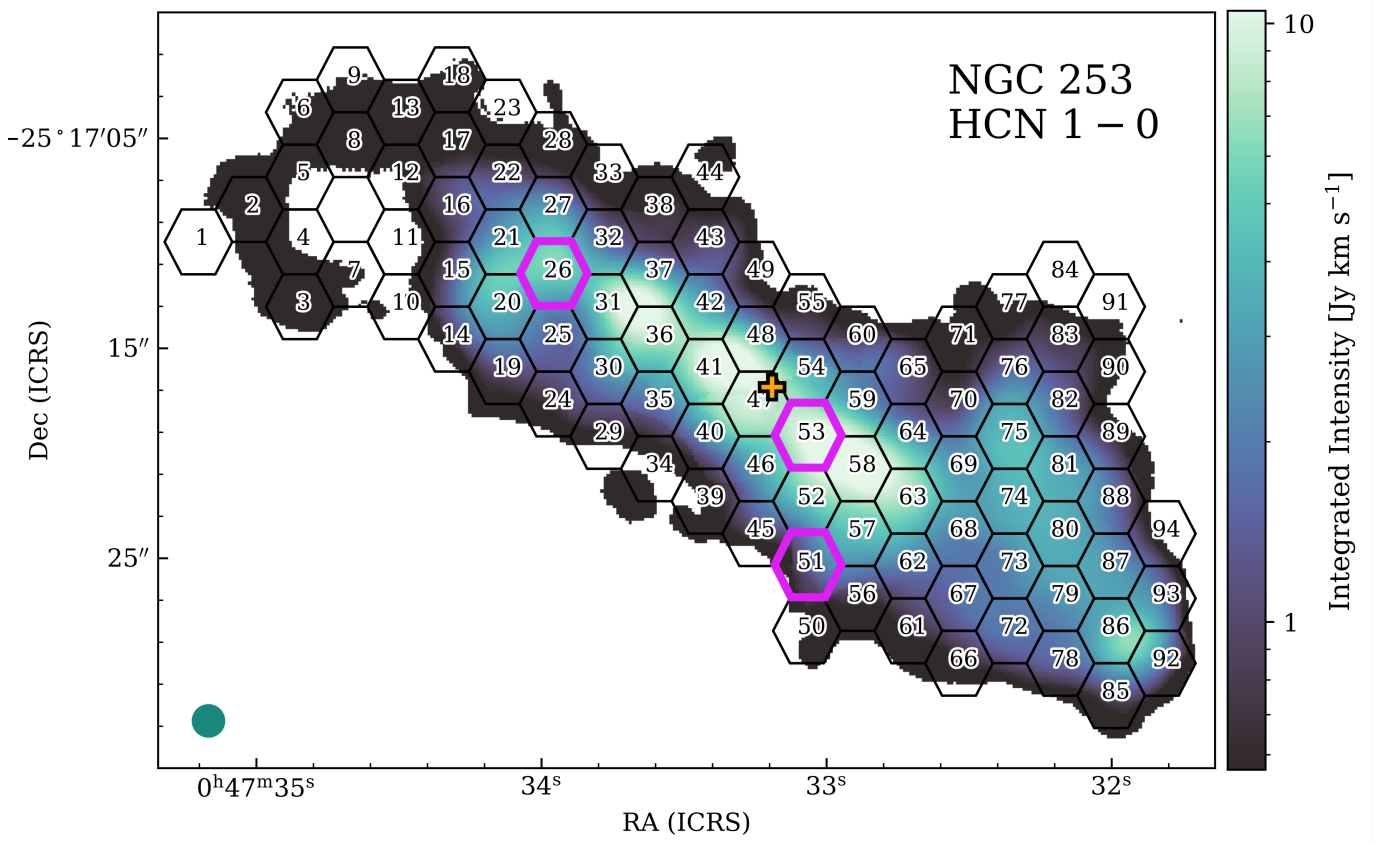


Figure 1. Map of NGC 253 HCN 1–0 integrated emission with $S/N > 3$ overlaid with the regions analyzed in E. Behrens et al. (2024). The three regions analyzed in this paper are highlighted in purple. The circle in the bottom left corner indicates the size of the $1.^{\prime\prime}6$ (~ 27 pc) ALCHEMI beam. The orange cross indicates the location of the galaxy's kinematic center (J. L. Turner & P. T. P. Ho 1985).

Table 3. Molecular Transition Combinations

# T	1 – 0		2 – 1		3 – 2		4 – 3	
	HCN	HNC	HCN	HNC	HCN	HNC	HCN	HNC
1	♦	-	-	-	-	-	-	-
	-	♦	-	-	-	-	-	-
	-	-	♦	-	-	-	-	-
	-	-	-	♦	-	-	-	-
	-	-	-	-	♦	-	-	-
	-	-	-	-	-	♦	-	-
	-	-	-	-	-	-	♦	-
	-	-	-	-	-	-	-	♦
2	✗	✗	-	-	-	-	-	-
	-	-	✗	✗	-	-	-	-
	-	-	-	-	✗	✗	-	-
	-	-	-	-	-	-	✗	✗
4	✗	✗	✗	✗	-	-	-	-
	✗	✗	-	-	✗	✗	-	-
	✗	✗	-	-	-	-	✗	✗
	-	-	✗	✗	✗	✗	-	-
	-	-	✗	✗	-	-	✗	✗
	-	-	-	-	✗	✗	✗	✗
	■	-	■	-	■	-	■	-
5	●	●	●	-	●	-	●	-
	●	●	-	●	-	●	-	●
	●	-	●	-	●	-	●	●
	-	●	-	●	-	●	●	●
6	✗	✗	✗	✗	✗	✗	-	-
	✗	✗	✗	✗	-	-	✗	✗
	✗	✗	-	-	✗	✗	✗	✗
	-	-	✗	✗	✗	✗	✗	✗
7	-	▲	▲	▲	▲	▲	▲	▲
	▲	-	▲	▲	▲	▲	▲	▲
	▲	▲	-	▲	▲	▲	▲	▲
	▲	▲	▲	-	▲	▲	▲	▲
	▲	▲	▲	▲	-	▲	▲	▲
	▲	▲	▲	▲	▲	-	▲	▲
	▲	▲	▲	▲	▲	▲	-	▲
	▲	▲	▲	▲	▲	▲	▲	-
8	✗	✗	✗	✗	✗	✗	✗	✗

♦ Single HCN OR HNC transition

✗ Matched HCN and HNC transitions

■ All HCN OR all HNC transitions

● All HCN with one HNC transition OR all HNC with one HCN transition

▲ Single HCN or HNC transition removed

which we compare our models and measurements does not account for the number of constraints. Thus we use upper limits to maintain common dimensionality across regions. Due to the low level of emission from these undetected transitions, and thus the low 3σ limits, they do not significantly contribute to our inference of the gas parameters (see Figure 11). Nevertheless, using 3σ upper limits prevents the model from invoking unrealistically high intensities for these transitions in the absence of constraints. The transitions that are replaced with this intensity limit have the lowest SNRs of any used in this study and will provide useful information describing how marginally-detected lines influence gas parameter constraints.

3.4. Molecular Constraints

We test several combinations of HCN and HNC transitions sampled from the first four HCN and HNC vibrational-ground rotational transitions: $J = 1 – 0$, $2 – 1$, $3 – 2$, and $4 – 3$. Table 3 shows a comprehensive list of the transition combinations we test and categorizes them into several groupings, which we will discuss here.

We first test the constraining power of single transitions when inferring gas parameters. These cases are marked with the ♦ symbol in Table 3 and utilize only one HCN or HNC transition to determine the gas conditions. In both nearby and high-redshift galaxies, oftentimes only one or two transitions, such as the HCN $J = 1 – 0$ and $J = 3 – 2$, are used to infer gas conditions such as volume density or dense gas mass (J. S. Spilker et al. 2014; I. Oteo et al. 2017; M. Rybak et al. 2022). We will consider the efficacy of using a single transition to constrain the molecular gas conditions and provide quantitative benchmarks that evaluate their accuracy in inferring gas parameters.

We then consider the case of matched HCN and HNC transitions (✗-marked combinations), i.e. when we test the effects of constraining models with just the $J = 1 – 0$ transition, we are using both the HCN and HNC $J = 1 – 0$ transitions together. Previous studies (E. Behrens et al. 2022, 2024) have shown that the combination of HCN and HNC measurements, rather than just one species alone, is necessary in order to obtain clear constraints on certain model parameters, such as the cosmic-ray ionization rate.

To further explore the necessity of using multiple species to constrain different gas parameters, we also test cases where all transitions from one species are used in combination with just a single transition of the other species (●-marked combinations). We choose either the $J = 1 – 0$ or $J = 4 – 3$ transitions to supplement the full set of the other species in order to determine whether the excitation level of the single additional transition affects the efficacy of using two species to constrain the gas conditions. We will compare these tests to the cases where we use all the transitions of a single species (■-marked

combinations in Table 3) to determine both how well various gas conditions can be constrained with a single species as well as whether the addition of a single transition from another species improves these constraints.

We also test whether any one transition has a particularly enhanced ability to constrain the physical parameters. We explore how removing a single transition from the full set of 8 affects our results (\blacktriangle -marked combinations) to determine whether any one transition should be included in the constraints.

Using each combination of HCN and HNC transitions listed in Table 3, we run our Bayesian inference plus neural network algorithm (described in Section 3.2) to obtain posterior distributions for each parameter listed in Table 2. Example corner plots for each combination type can be found in Appendix A for the low- n - ζ region. We compare the posterior distributions from each test case for each parameter to those obtained when using all eight transitions as constraints (see Table 2), which we will hereafter refer to as the “control distributions”. Note that, as with all modeling frameworks, we cannot know with complete certainty that our model includes all of the physical and chemical processes occurring in a studied region, and thus we do not know if the parameters inferred from our set of control measurements are completely correct. However, our purpose with this study is instead to quantify how our understanding of the gas parameters may change when we use a different number of constraining measurements to infer said parameters.

To compare the test and control cases, we employ least-squares residuals. We do this by first binning the test and control distributions using the Freedman-Diaconis rule based on the data in the control distribution. This rule states that the bin width should be equal to $2 \times IQR \times N^{-1/3}$, where IQR is the interquartile range (which is calculated in logarithmic space) and N is the number of data points in the control distribution. We use identical bins for control and test distributions, which contain similar numbers of data points. We then calculate the residuals in each bin, sum them up, and normalize the final values to obtain a single residual r for each test distribution using the following expression:

$$r = \sum_{i=1}^n \left(\frac{k_i}{N_{\text{control}}} - \frac{j_i}{N_{\text{test}}} \right)^2, \quad (2)$$

where k and j are the number of samples in the i th bin of the control and test distributions, respectively, and N is the number of total samples in each distribution.

3.5. Bayesian Inference Under Idealized Conditions

To confirm that any differences in the inferred parameters arise solely from the constraining transitions and not from the Bayesian inference algorithm, we consider Bayesian inference results under idealized conditions with synthetic data. We generate synthetic data

for a region with conditions mirroring those in the high- n - ζ region by taking the inferred parameters for the high- n - ζ region from Table 2 and running them through our neural network and radiative transfer models to generate synthetic integrated intensities. We divide these integrated intensities by 3 and 5 to generate uncertainties that result in synthetic measurements with SNRs of 3 and 5, respectively. We then use various combinations of these synthetic integrated intensity and uncertainty values to constrain the Bayesian inference algorithm with the intention of recovering the same parameter values that were used to generate the synthetic data.

Figure 2 shows the results of constraining models with the 8 HCN and HNC transitions (the control) measured toward the high- n - ζ region, as well as the results obtained from synthetic constraints with SNRs of 3 and 5. These results are also shown in Table 4, along with results for the same regions for models constrained with just HCN 1 – 0 and just the four HNC transitions. Figures for the HCN 1 – 0 and HNC only tests can be found in Appendix A. Tests with the synthetic data show that the Bayesian inference algorithm successfully recovers the input high- n - ζ region gas parameters. Synthetic measurements with $\text{SNR} = 5$ result in better constrained gas parameters than in the $\text{SNR} = 3$ case, with smaller uncertainties and median parameter values that more closely match those obtained with the high- n - ζ measured transitions. However, all median parameter values inferred from both the $\text{SNR} = 3$ and $\text{SNR} = 5$ tests fall within the uncertainty range set by the high- n - ζ results. These tests indicate that any changes seen in the inferred gas parameters are a result of the combination and/or the SNR of the constraining transitions, not the Bayesian inference algorithm.

4. RESULTS

In the following we will describe the results of our HCN and HNC measurement constraints investigation. The normalized residuals for each test case and parameter are shown in Figures 3, 4, and 5 for the low- n - ζ , high- n - ζ , and low-SNR regions, respectively. For each region, we collect the residuals across all parameters and calculate quartiles, which provide three thresholds (quartile 1, or Q1; the median, r_{med} ; and quartile 3, or Q3) that separate the transition combinations into four groups based on the residuals. We will use these delineations in the following discussion to evaluate the efficacy of each combination’s ability to reproduce the control distributions.

Examples of test combination posterior distributions that fall between each quartile are shown in Figure 6 as compared to the control for volume density in the low- n - ζ region. Test combinations with residuals $r < Q1$ are generally nearly indistinguishable from the control distributions. Transition combinations with $Q1 < r < r_{\text{med}}$ typically recover the same median value of the posterior

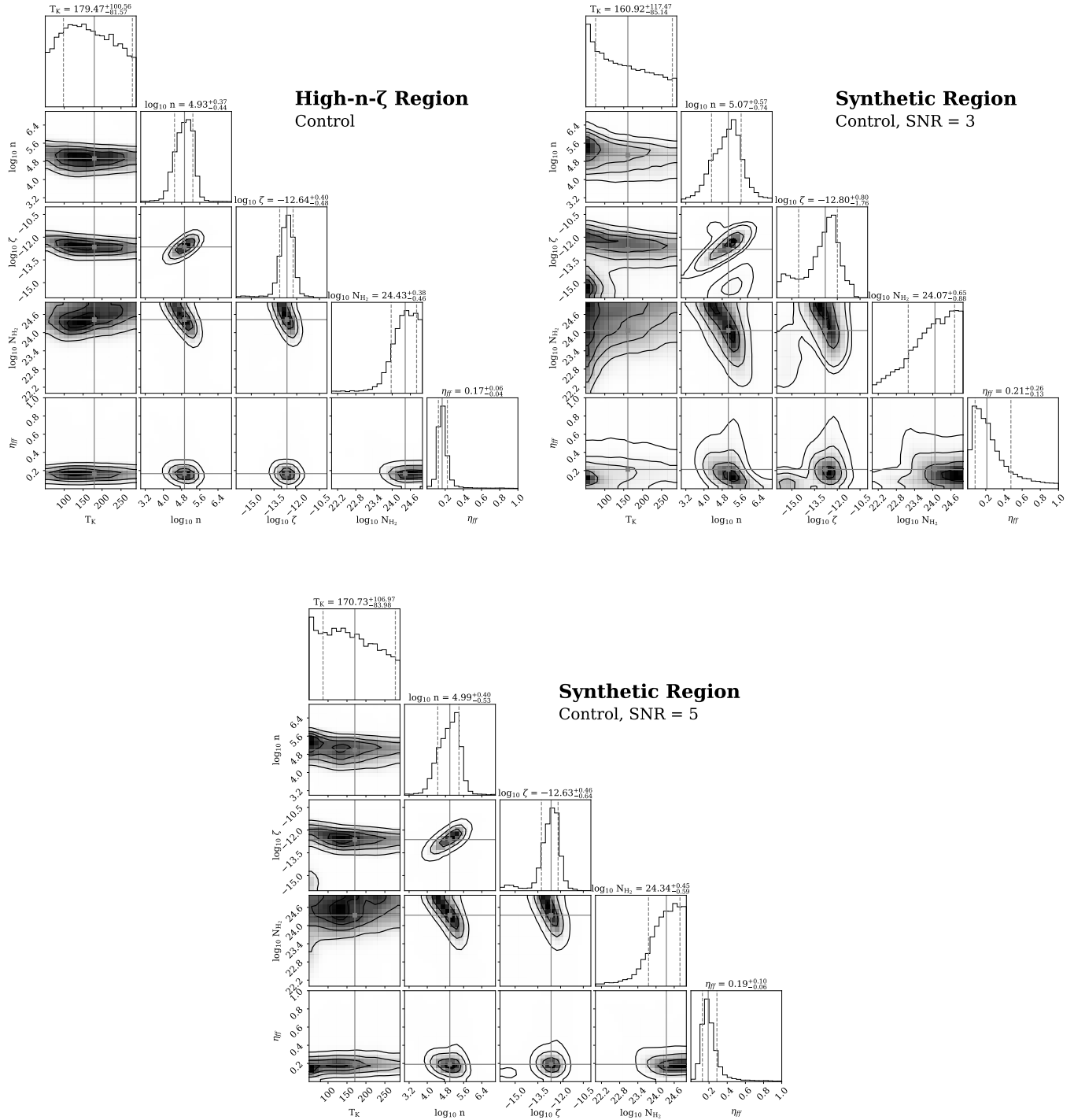


Figure 2. Bayesian inference results for the controls of the high- n - ζ region (top left) and for the synthetic region where the synthetic data SNR = 3 (top right) and SNR = 5 (bottom).

Table 4. Inferred Parameter Values for Observationally and Synthetically Constrained Models

	Region	T_K (K)	n_{H_2} (cm $^{-3}$)	ζ (s $^{-1}$)	N_{H_2} (cm $^{-2}$)	η_{ff}
Control	High- $n\text{-}\zeta$	$179.47^{+100.56}_{-81.57}$	$4.93^{+0.37a}_{-0.44}$	$-12.64^{+0.40a}_{-0.48}$	$24.43^{+0.38a}_{-0.46}$	$0.17^{+0.06}_{-0.04}$
	Synthetic, SNR = 3	$160.92^{+117.47}_{-85.14}$	$5.07^{+0.57a}_{-0.74}$	$-12.80^{+0.80a}_{-1.76}$	$24.07^{+0.65a}_{-0.88}$	$0.21^{+0.26}_{-0.13}$
	Synthetic, SNR = 5	$170.73^{+106.97}_{-83.98}$	$4.99^{+0.40a}_{-0.53}$	$-12.63^{+0.46a}_{-0.64}$	$24.34^{+0.45a}_{-0.59}$	$0.19^{+0.10}_{-0.06}$
HCN 1-0	High- $n\text{-}\zeta$	$199.09^{+101.42}_{-101.74}$	$4.43^{+1.63a}_{-0.92}$	$-12.91^{+1.42a}_{-2.04}$	$23.28^{+1.06a}_{-0.81}$	$0.46^{+0.36}_{-0.32}$
	Synthetic, SNR = 3	$196.68^{+102.46}_{-102.14}$	$4.38^{+1.61a}_{-0.89}$	$-12.78^{+1.34a}_{-2.05}$	$23.29^{+1.07a}_{-0.85}$	$0.44^{+0.37}_{-0.31}$
	Synthetic, SNR = 5	$199.97^{+101.23}_{-103.25}$	$4.43^{+1.63a}_{-0.90}$	$-12.91^{+1.41a}_{-2.05}$	$23.31^{+1.08a}_{-0.83}$	$0.44^{+0.36}_{-0.32}$
HNC only	High- $n\text{-}\zeta$	$221.51^{+90.36}_{-110.47}$	$4.95^{+0.36a}_{-0.51}$	$-14.10^{+1.69a}_{-1.29}$	$24.00^{+0.71a}_{-0.89}$	$0.18^{+0.15}_{-0.06}$
	Synthetic, SNR = 3	$210.58^{+97.05}_{-106.41}$	$5.03^{+0.59a}_{-0.75}$	$-13.80^{+1.92a}_{-1.48}$	$23.77^{+0.83a}_{-1.02}$	$0.37^{+0.37}_{-0.21}$
	Synthetic, SNR = 5	$217.11^{+92.70}_{-108.66}$	$5.02^{+0.36a}_{-0.58}$	$-13.97^{+1.69a}_{-1.39}$	$23.89^{+0.77a}_{-0.96}$	$0.25^{+0.24}_{-0.10}$

^aValue is given in logspace

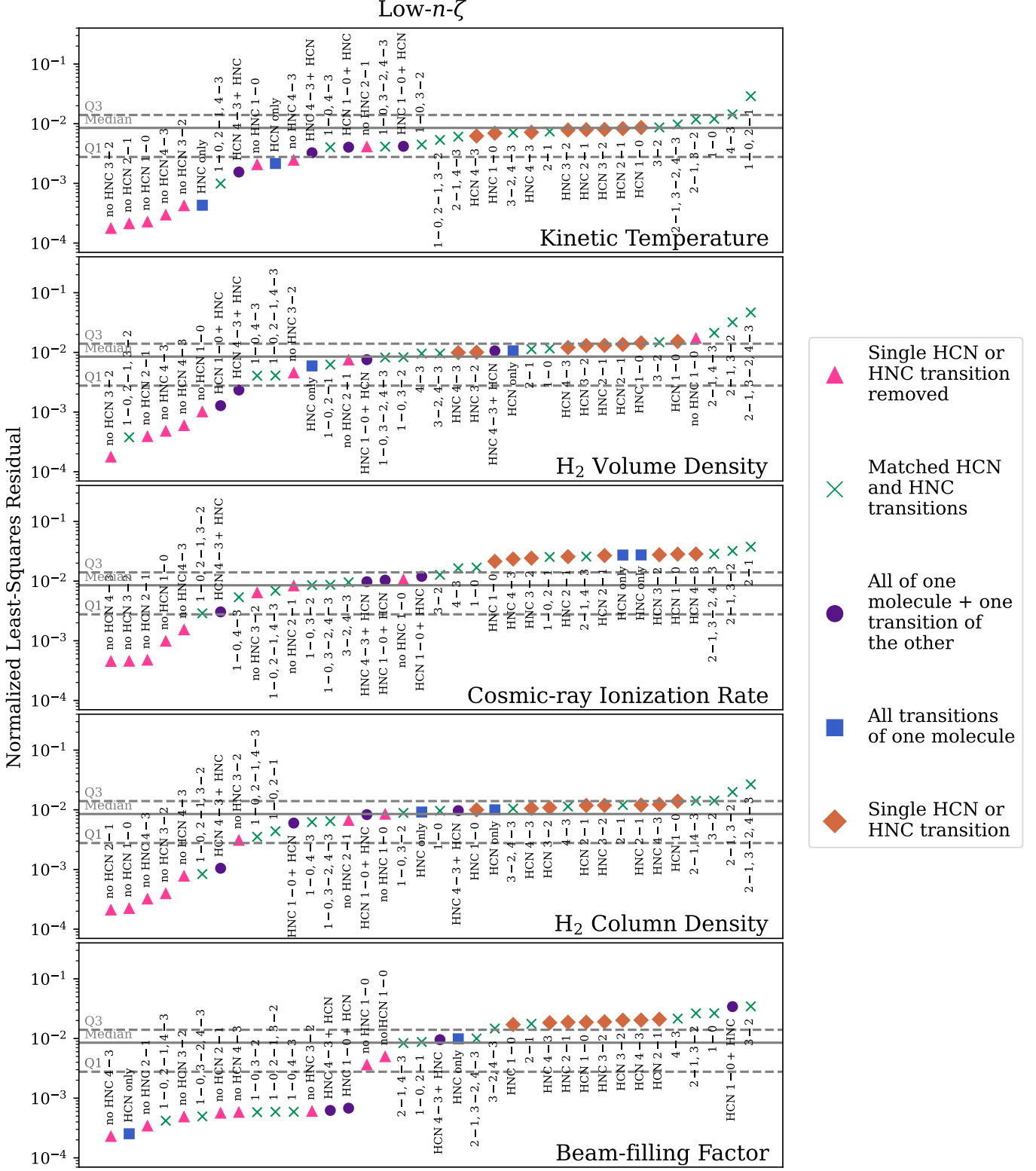


Figure 3. Normalized least-squares residuals for each transition combination listed in Table 3, where residual values close to zero indicate better agreement between the test and control distributions. The solid gray lines represent the median residual value across all parameters for the low- $n\zeta$ region, and the dashed gray lines represent the first and third quartiles.

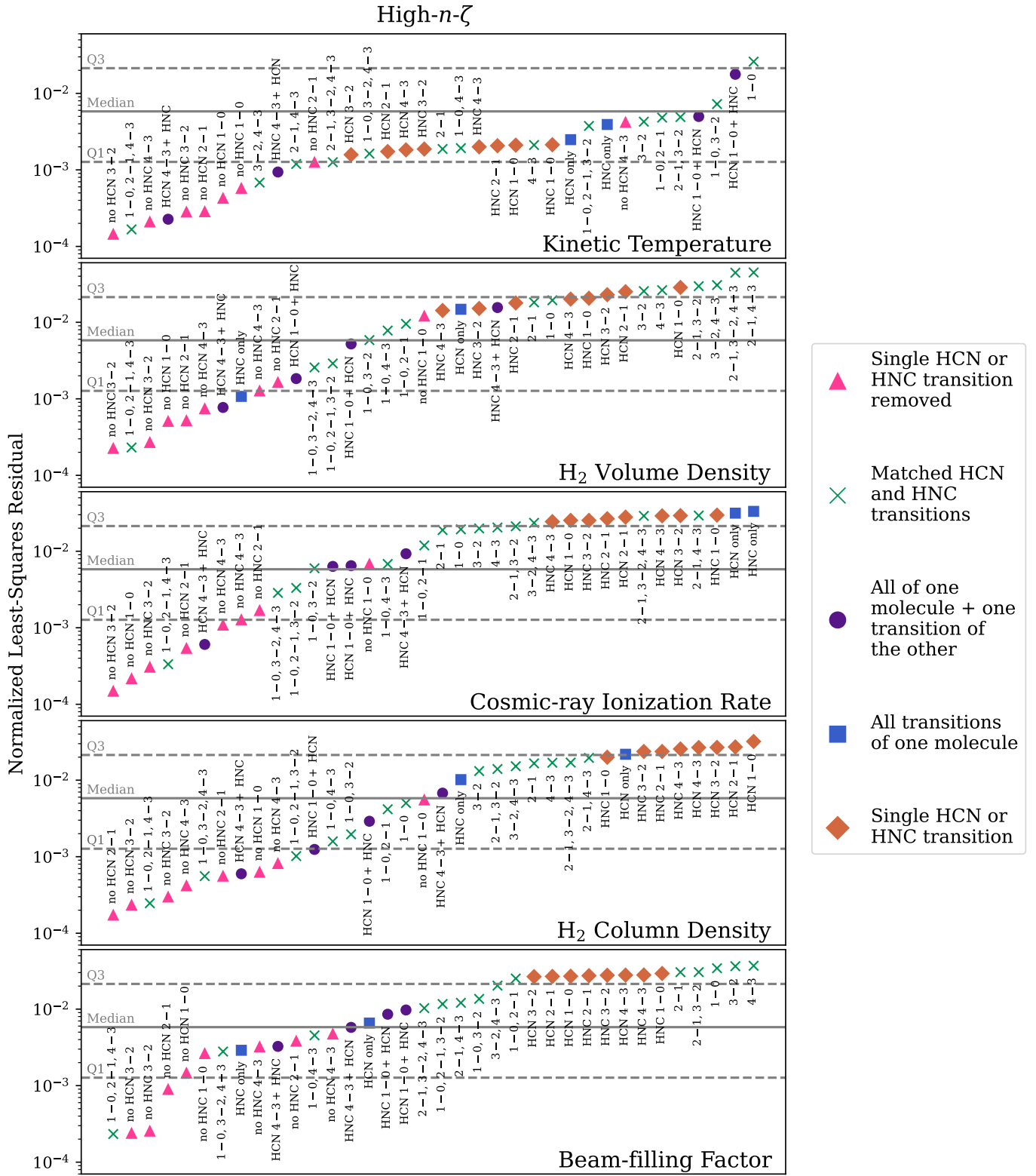


Figure 4. Same as in Figures 3 and 5 but for the high- $n\zeta$ region.

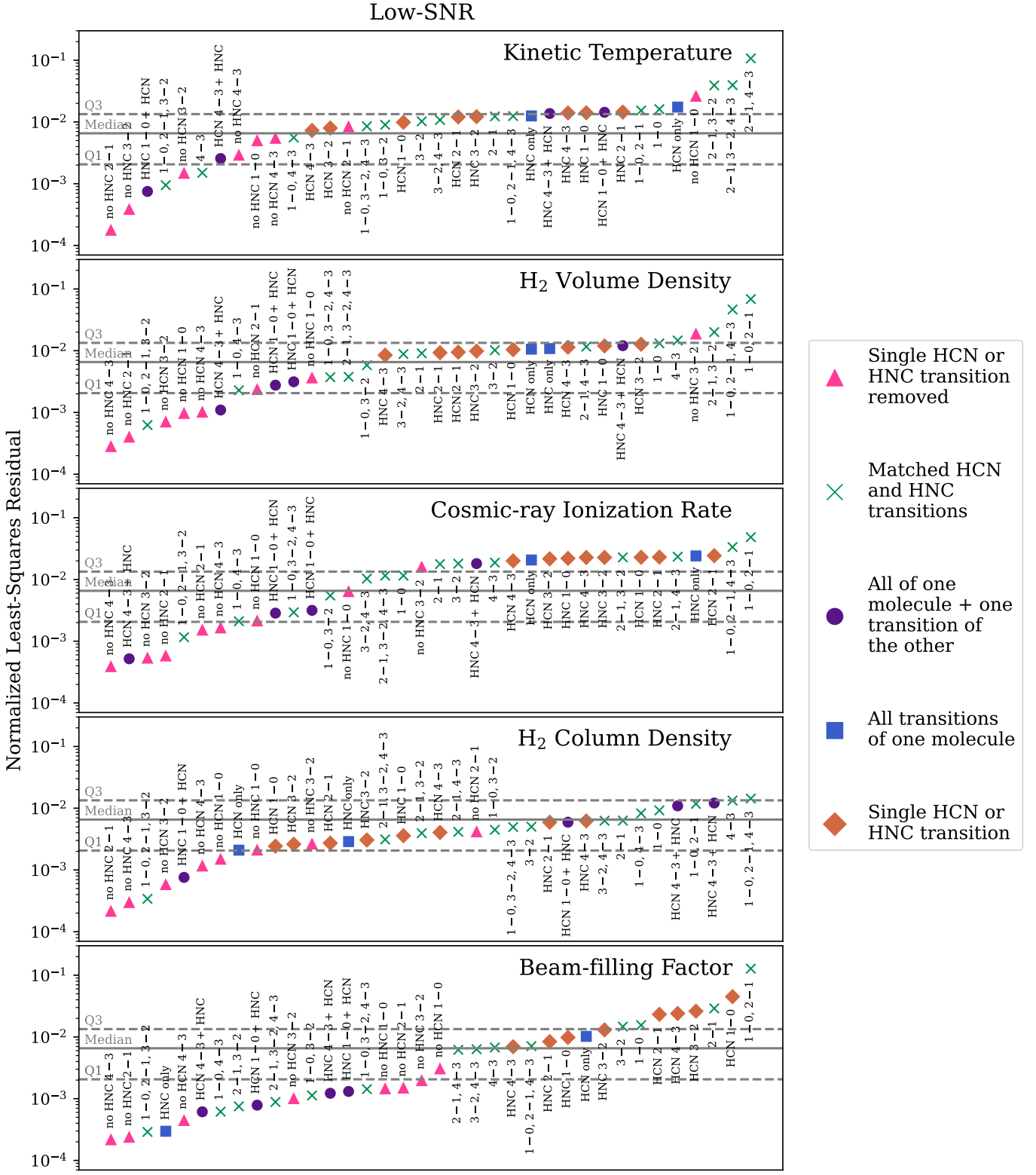


Figure 5. Same as in Figure 3 but for the low-SNR region.

distribution as the control and usually have similar uncertainties. It is thus up to the user to determine to what accuracy and precision threshold a given combination must rise in order to meet the requirements of their use case. Note, however, that these quartile values describe only where each transition combination falls with respect to the other combinations we describe in Section 3.4, which are not necessarily representative of all possible combinations of the HCN and HNC $J = 1 - 0$, $2 - 1$, $3 - 2$, and $4 - 3$ transitions. We will address each transition grouping, as described in Section 3.4 and Table 3, separately and then synthesize these results in Section 5.

4.1. Single Transitions

We first consider the test cases in which we used a single HCN or HNC transition to constrain the models used in our Bayesian inferencing algorithm. These test cases are denoted in Figures 3, 4, and 5 with the ♦ symbol. In general, we caution readers against using single transitions to infer any physical parameters, as the degeneracy between key gas parameters (e.g. density and temperature) results in extremely uncertain or inaccurate parameter estimates. In nearly all cases, constraining the gas conditions with a single HCN or HNC transition resulted in residual values greater than the median residual for every parameter in each respective region. The only exceptions are for kinetic temperature in the low- and high- $n\zeta$ regions and H₂ column density in the low-SNR region. As mentioned in Section 3.2, we are unable to constrain the kinetic temperature in this environment with HCN and HNC measurements; thus we expect that any trends we note regarding the constraining power of HCN and HNC will likely not hold for kinetic temperature. We will further discuss any discrepancies in trends in the low-SNR region in Section 5.

In general, higher- J ($J = 3 - 2$ or $4 - 3$) single transitions are more effective at reproducing the control distributions across all regions than lower- J transitions. Though the differences in residuals between the single-transition cases are often minimal, the most effective single-transition tests use the HCN or HNC $J = 3 - 2$ or $4 - 3$ transitions in two-thirds of cases. HNC is also slightly more effective than HCN at reproducing control distributions when a single transition is used, with 60% of cases featuring an HNC transition as the single-transition test with the lowest residual value. Alternatively, low-energy HCN and HNC transitions are among the least effective in reproducing the control posterior distributions. In particular, the HCN $J = 1 - 0$ transition results in residual values that are above the third quartile in two-thirds of cases.

4.2. Matched HCN and HNC Transitions

Matched transitions, which use the same HCN and HNC transitions to constrain each model, are denoted in Figures 3, 4, and 5 with ✕ symbols. Since the

single-transition tests (Section 4.1) indicate that higher- J transitions are better at reproducing the control posterior distributions, we consider the same scenario for the matched-transition test cases. Across the three regions we test, the matched-transition test cases with the lowest residual values for each parameter contain either the HCN and HNC $J = 3 - 2$ or $4 - 3$ transitions.

To further investigate the impact of higher-energy transitions on our ability to constrain gas parameters, we show in Figure 7 how starting with just the HCN and HNC $J = 1 - 0$ transitions and progressively adding matched sets of higher-energy transition constraints affects the parameter posterior distributions for each parameter in the low- $n\zeta$ region. In the case of volume density, which our control indicates is $\sim 10^4 \text{ cm}^{-3}$, a posterior distribution with a similar median and uncertainty range to our control can be obtained with just the HCN and HNC $J = 1 - 0$ and $2 - 1$ transitions. Though using just the HCN and HNC $J = 1 - 0$ transitions recovers a median density within the uncertainty of our control, the uncertainty on the test case is much larger, spanning nearly two orders of magnitude. On the other hand, Figure 7 shows that an accurate estimate of the CRIR with reasonable uncertainty cannot be achieved until the $J = 4 - 3$ HCN and HNC transitions are included. This particular CRIR posterior distribution example features a bimodality (discussed in E. Behrens et al. 2022) that cannot be fully resolved without the addition of higher- J transitions.

However, we see from Figures 3, 4, and 5 that reasonable constraints that mirror the control CRIR posterior distributions can be obtained without all 8 HCN and HNC transitions. The matched-transition tests with the lowest residuals for CRIR across all regions contained the $J = 1 - 0$, $2 - 1$, and either the $3 - 2$ or $4 - 3$ HCN and HNC transitions. These results show that a combination of low- and high-energy molecular transitions from both HCN and HNC can reliably reproduce the control posterior distributions without requiring all 8 of the transitions used in the control.

The combinations of transitions that ultimately prove to provide the best constraints on the physical conditions may be dependent upon the specific conditions of the region under study. In the low- $n\zeta$ region (Figure 3), the most effective matched-transition combination to recover the volume density control posterior distribution ($n \sim 10^4 \text{ cm}^{-3}$) is the $J = 1 - 0$, $2 - 1$, and $3 - 2$ combination, which has a residual that falls well below the first quartile. Alternatively, replacing the $J = 3 - 2$ transitions with the $J = 4 - 3$ transitions yields a higher residual, between the first quartile and the median. However in the high- $n\zeta$ region, which the control indicates has a higher volume density ($\sim 10^5 \text{ cm}^{-3}$), the $J = 1 - 0$, $2 - 1$, and $4 - 3$ transition combination is most effective at recovering the volume density with a residual below the first quartile, while swapping the $J = 4 - 3$ transitions for the $J = 3 - 2$ would result in a higher resid-

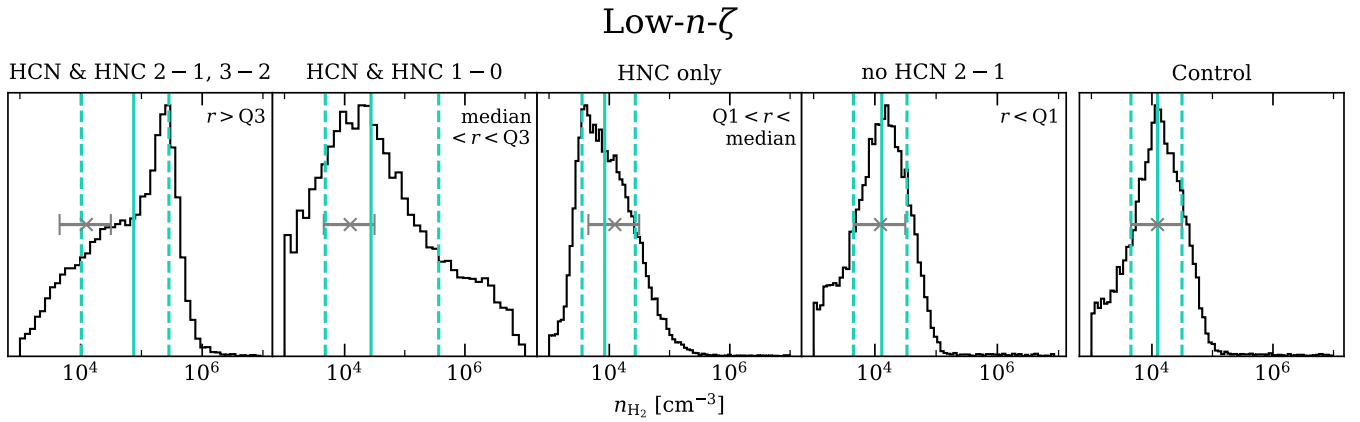


Figure 6. Example volume density posterior distributions for transition combinations that fall above, below, and between the three quartiles in the low- $n\zeta$ region. Teal lines indicate the median (solid) and middle 66% (dashed) of each distribution, while the gray X's and horizontal errors bars show the median and middle 66%, respectively, of the control distribution (right panel).

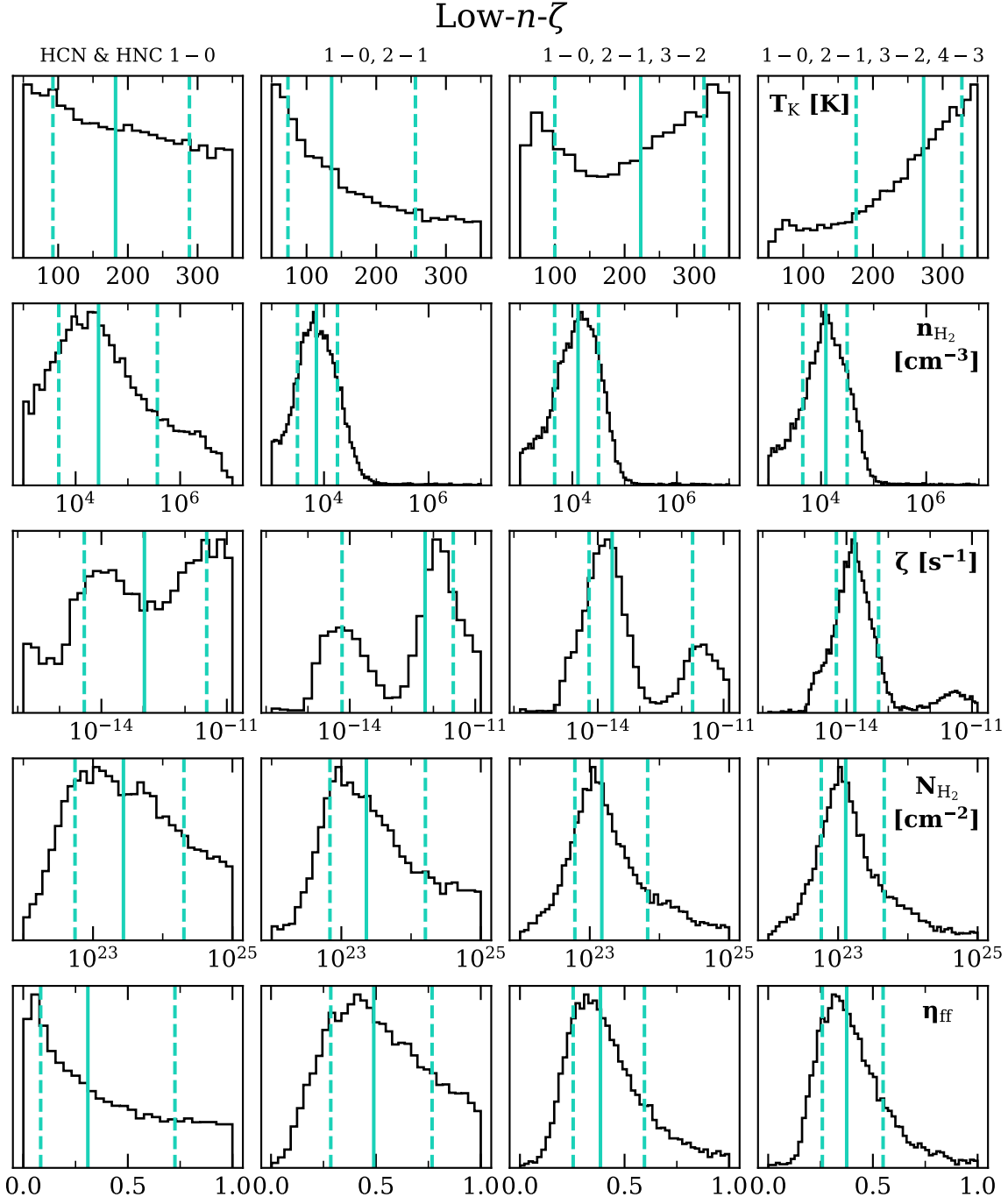


Figure 7. One-dimensional posterior distributions for the low- $n\zeta$ region constrained by an increasing number of higher- J HCN and HNC transitions. Median values for each distribution are denoted by the solid lines, and the middle 66% of the distribution is indicated by the dashed lines.

ual between the first quartile and median. Both combinations are generally effective, but the volume density posterior distribution is better recovered when using the highest-energy transitions in this higher-density region. We note that in the case of the low-SNR region, though the $J = 1 - 0$, $2 - 1$, and $3 - 2$ combination performs quite well across all parameters, the $J = 1 - 0$, $2 - 1$, and $4 - 3$ combination is actually one of the worst. This discrepancy may be a result of the lower SNR of the transitions measured in this region, which often results in less stable parameter constraints.

We also see that the inclusion of the $J = 1 - 0$ HCN and HNC transitions is important for recovering the control distributions. Combinations that do not include the $J = 1 - 0$ transitions, even when including the other 6 transitions, almost exclusively result in residuals higher than the median and rank behind almost all other tested combinations. When 6 transitions are used, we also see that including two sets of lower-energy transitions ($J = 1 - 0$ and $2 - 1$) and one higher-energy transition ($J = 3 - 2$ or $4 - 3$) is more effective than including only one lower-energy and two higher-energy pairs. We will discuss these results further in Section 5.

4.3. Single Species

Models that we constrain with all four transitions of a single species are shown in Figures 3, 4, and 5 with ■ symbols. Single-species constraints generally only yield posterior distributions that resemble the control in the case of volume density, and only for a specific subset of cases. In the low- $n\zeta$ region, the HNC-only test yields a residual value between the first quartile (Q1) and the median for H_2 volume density, and in the high- $n\zeta$ region, the same test results in a residual value below Q1. Alternatively, the HCN-only test case results in residual values greater than the median in all regions for volume density, indicating that HNC by itself may be more useful for constraining the gas density than HCN. Using a single species to constrain our models results in very inaccurate and ineffective constraints on the cosmic-ray ionization rate and inconsistent results for all other parameters across all three regions.

4.4. Single Species with One Opposing Species Transition Added

The test cases where we have used all the transitions from one species with one additional high- or low-energy transition from the opposing species are shown with ● symbols in Figures 3, 4, and 5. In nearly all cases, the ● test with the lowest residual value for each parameter includes all HNC transitions with one additional HCN transition. In the high- $n\zeta$ region, supplementing the HNC transitions with a single HCN transition results in posterior distributions with residual values below Q1 for all parameters except the beam-filling factor. In the low- and high- $n\zeta$ regions, using the HCN $J = 4 - 3$ transition to supplement the HNC constraints, rather

than the HCN $J = 1 - 0$, is more effective at recovering the control distributions across all parameters, except the beam-filling factor in the low- $n\zeta$ region. The results are less consistent in the low-SNR region, which shows a mix of favoring the HNC + HCN $J = 4 - 3$ combination as well as HCN + HNC $J = 1 - 0$ for the most effective test cases in this category. In general, adding one transition from a different species results in significant improvements in the posterior distributions compared to using only transitions from a single species. Using a higher-energy transition as the supplementary constraint may further improve results.

4.5. Removing a Single Transition

In order to assess whether any single transition has a significant impact on the gas parameter constraints, we try removing one transition at a time from our measurement constraints, which are denoted by ▲ symbols in Figures 3, 4, and 5. These results show that the HNC $J = 1 - 0$ transition has the largest impact on our parameter inferencing results. While most tests in this category result in residuals below Q1, removing the HNC $J = 1 - 0$ transition from our constraints often leads to residual values greater than the median. This result is especially evident for volume density in the low- and high- $n\zeta$ regions, where significant gaps exist between this case and all other ▲ test cases. The low-SNR region is less consistent, with a variety of other transitions appearing to be the most impactful on the parameter inferencing results. Other parameters do not show significant preferences toward any particular transition.

5. DISCUSSION

5.1. Quantifying the Efficacy of Transition Constraints Tests

In Section 4 we described how well each category of transition constraints performed in reproducing the control gas parameter posterior distributions that utilize all eight HCN and HNC transitions measured toward NGC 253 by the ALCHEMI Large Program. To aid observers in choosing the transition combinations that suit their needs, we consider an additional metric for evaluating the performance of each test case and compare this metric to the results obtained by calculating posterior distribution residuals.

This metric separates the accuracy (how close a test median is to the control median) and precision (how much larger the test uncertainty is than the control) of the posterior distribution results for each test case so that observers may choose the HCN and HNC combinations most suited to their science case. We first calculate the fractional difference between the median values of each gas parameter derived from each test case, M_{test} , to the median gas parameter values derived from the control distributions, M_{ctrl} , for each of the three regions. We calculate the fractional difference between M_{test} and M_{ctrl} , which is given by $(M_{\text{test}} - M_{\text{ctrl}})/M_{\text{ctrl}}$. Note

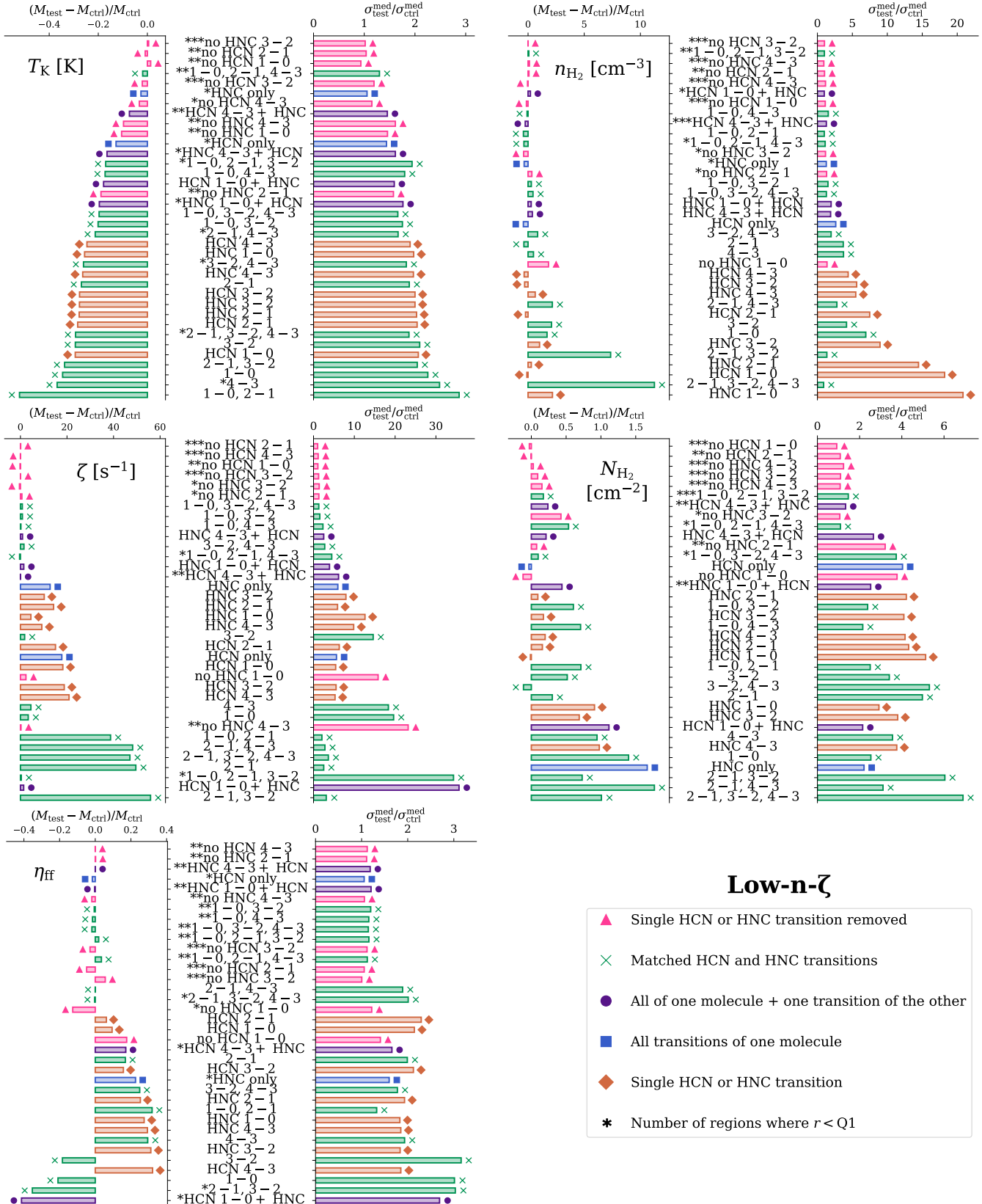


Figure 8. Fractional difference between the test and control medians for each test combination as well as ratio of test to control uncertainty in the low- $n\zeta$ region for T_K (top left), n_{H_2} (top right), ζ (middle left), N_{H_2} (middle right), and η_{ff} (bottom left). Number of asterisks (*) next to each test combination represents the number of regions for which that combination's calculated residual value was below Q1.

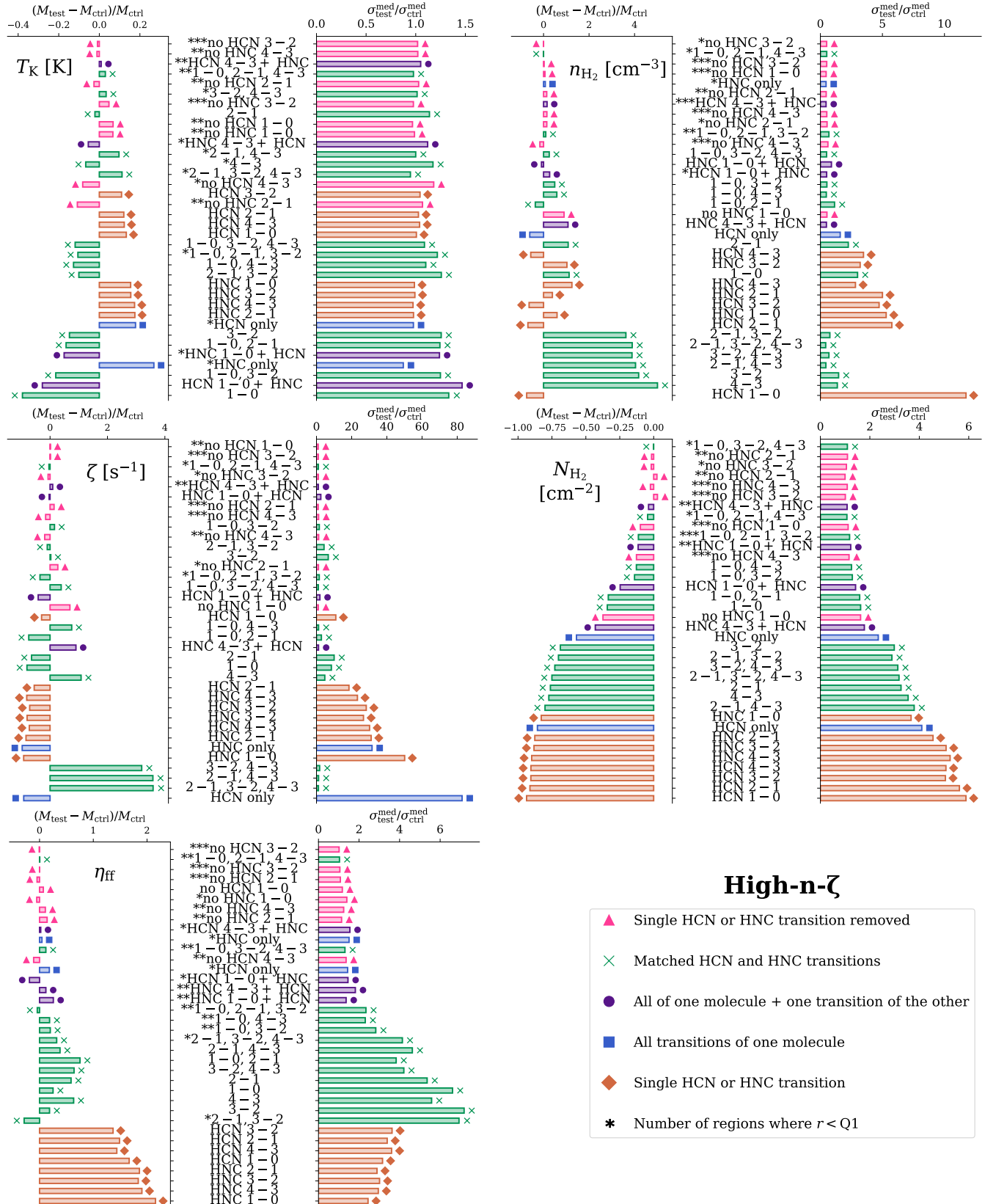


Figure 9. Same as in Figure 8 but for the high- n - ζ region.

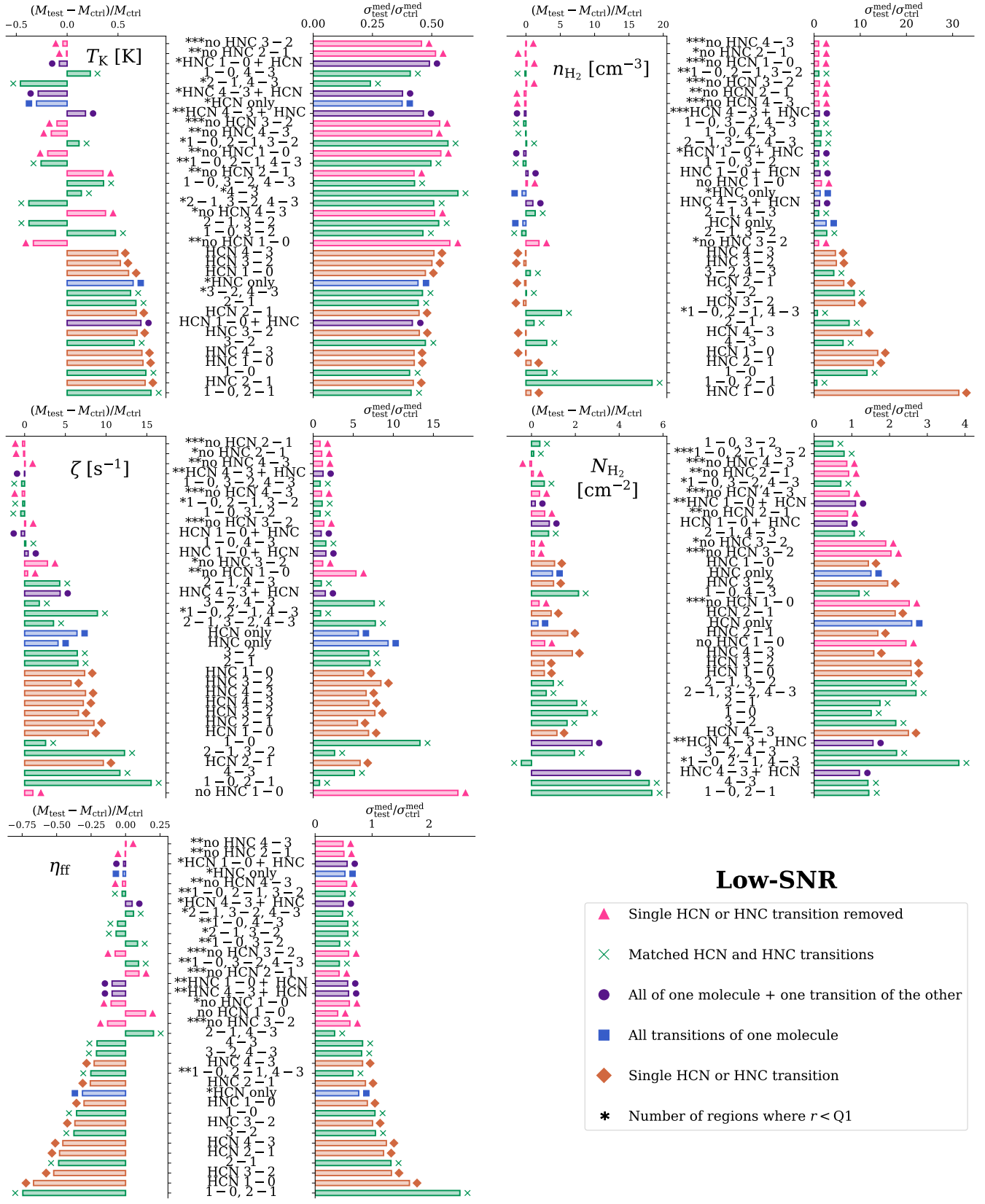


Figure 10. Same as in Figures 8 and 9 but for the low-SNR region.

that we calculate these values in linear space, even for the three gas parameters for which we use log-uniform distributions in our modeling (n_{H_2} , ζ , and N_{H_2}).

To evaluate the precision of each test case in constraining our five gas parameters, we consider the ratio of the median-weighted test uncertainty to the median-weighted control uncertainty, $\sigma_{\text{test}}^{\text{med}}/\sigma_{\text{ctrl}}^{\text{med}}$, where $\sigma^{\text{med}} \equiv \sigma/M$ for both the control and test fit uncertainties. As with the median fractional difference, we calculate the median-weighted uncertainty ratio values within each of the three regions for each gas parameter and test case. The results of both the accuracy and precision metrics are shown in Figures 8, 9, and 10. We have ordered the transition combination test cases according to their total bar length (see Figures 8, 9, and 10), which is given by

$$\text{Tot. bar length} = \frac{\Delta M/M_{\text{ctrl}}}{(\Delta M/M_{\text{ctrl}})_{\text{max}}} + \frac{\sigma_{\text{test}}^{\text{med}}/\sigma_{\text{ctrl}}^{\text{med}}}{(\sigma_{\text{test}}^{\text{med}}/\sigma_{\text{ctrl}}^{\text{med}})_{\text{max}}}, \quad (3)$$

where ΔM is the difference between the test and control medians, and $(\Delta M/M_{\text{ctrl}})_{\text{max}}$ and $(\sigma_{\text{test}}^{\text{med}}/\sigma_{\text{ctrl}}^{\text{med}})_{\text{max}}$ are the maximum values for the median and uncertainty metrics for a given gas parameter and region. The test cases with the smallest total bar lengths, and thus the closest analogs to the control distributions according to these metrics, are at the top of each panel, while the worst cases are located at the bottom.

These metrics, presented in Figures 8, 9, and 10, largely echo the results presented in Section 4. As noted earlier, we do not constrain kinetic temperature well in any of these regions even with the control. Nevertheless, the results from the temperature panels reflect the results seen in other parameters. The best analogs to the controls are unsurprisingly the combinations where only a single transition has been removed. In the case of volume density, the top half of transition combinations will generally yield a median parameter value within a factor of two and an uncertainty less than five times that of the control. The worst cases for volume density constraint consist mostly of matched transitions (green X) that either did not include the $J = 1 - 0$ transitions or poorly sampled the upper-state energy ladder and single transitions (red ♦). These combinations may still yield a median value within a factor of 2–5 of the control, but the uncertainties are much larger, 5–10 times larger than the control uncertainties. For the CRIR, the results worsen significantly when only one molecule is used to constrain our models. Combinations that use a single transition (red ♦) or single molecule (blue ■) either overestimate the median by a factor of ~ 20 , in the case of the low- $n\zeta$ region (Figure 8), or have an uncertainty 20–50 times greater than that of the control, as is the case in the high- $n\zeta$ region (Figure 9). Most transition combinations yield a column density within a factor of two of the control median with uncertainties 1–6 times that of the control.

Finally, we see in the beam-filling factor plots that across all regions, using single transitions or matched transition combinations that do not appropriately sample the transition energy ladder result in poorer estimations of the beam-filling factor but still yield median values within a factor of 2–3 of the control median.

To tie in the results of Section 4, we also show in Figures 8, 9, and 10 the number of regions for which a given test combination yielded residuals below the Q1 threshold for each parameter using asterisks (*). For instance, in the ζ panel of Figure 8, the test combination that used all HCN and HNC transitions excluding the HCN $3 - 2$ yielded a residual below Q1 in all three regions for the CRIR, while the combination that used the $1 - 0$, $2 - 1$, and $4 - 3$ HCN and HNC transitions only resulted in residuals below the Q1 threshold in one region. Combinations near the top of a given panel in Figures 8, 9, and 10 with more than one asterisk are likely to be the most consistently useful across different environments when constraining a given parameter.

5.2. Signal-to-Noise Ratio

Our results demonstrate that parameter values inferred by the HCN and HNC measurements toward the low-SNR region are significantly less stable than those inferred toward the low- and high- $n\zeta$ regions. As noted in Section 3.3, we included the low-SNR region in our analysis to determine the impacts of molecular constraints with low SNRs on our parameter inferencing results. Five HCN and HNC transitions were detected toward the low-SNR region in NGC 253 with $\text{SNR} \geq 3$: HCN $J = 1 - 0$, $2 - 1$, and $3 - 2$ and HNC $J = 2 - 1$, and $3 - 2$. These transitions were detected with SNRs of ~ 6.6 , 6.1 , and 5.9 for HCN, respectively, and ~ 6.6 and 3.0 for HNC. Note that the maximum SNR of 6.6 across all transitions studied here is set by our flux calibration uncertainty of $15\% = 1/6.6$.

We note in Section 4 that the trends seen in the low- and high- $n\zeta$ regions are not always consistent with those seen in the low-SNR region. When discussing the matched HCN and HNC transition combinations in Section 4.2, we note that some of the combinations that prove to be the best in the other regions do not always yield low residuals in the low-SNR region. While matched transitions of $J = 1 - 0$, $2 - 1$, and $3 - 2$ perform well, $J = 1 - 0$, $2 - 1$, and $4 - 3$ perform quite poorly. This result is likely due to the fact that in the low-SNR region, this combination contains no transitions with higher energies than the $J = 2 - 1$ that have $\text{SNR} > 3$, as the HCN and HNC $J = 4 - 3$ transitions were not detected at this threshold and thus were replaced with SNR limits. In the case of the HCN and HNC $J = 1 - 0$, $2 - 1$, and $3 - 2$ combination, the HCN $J = 3 - 2$ transition was detected with a SNR of ~ 6 and thus provides the parameter inferencing algorithm with some reliable information on the intensity of higher-energy transitions.

5.3. *HCN versus HNC as gas condition tracers*

Our results indicate that the necessity for using HCN, HNC, or the two species together to infer gas conditions in star-forming environments may be dependent on the specific parameter one desires to constrain. The results presented in Section 4 and Figures 8, 9, and 10 indicate that for volume density, HNC may be a more useful constraint than HCN. Figures 8, 9, and 10 show that for volume density, HNC by itself (■) ranks higher than HCN by itself across all three regions. However, both combinations will result in a median volume density within a factor of two of the control median with comparable uncertainty relative to the control. Additionally, in the cases where all transitions of one species are supplemented with a single transition of the opposing species (●), using majority HNC transitions is more effective for constraining the gas volume density. Figure 8 shows that for the low- n - ζ region, HNC supplemented with the HCN $J = 1 - 0$ and then the $J = 4 - 3$ rank sixth and ninth, respectively, overall for gas density. Furthermore, the combination with four HNC transitions + HCN 4–3 results in a residual below Q1 in all three regions for volume density (Figure 3). On the other hand, HCN supplemented with the $1 - 0$ and $4 - 3$ HNC transitions rank seventeenth and eighteenth, respectively, in the low- n - ζ region. These results indicate that when using an unequal number of constraints from HCN and HNC, having more HNC transitions is beneficial for inferring the gas density. Note, however, that supplementing one species' four transitions with one transition of the other species almost always improves the density constraints compared to only using a single species.

HCN's utility for constraining gas conditions may lie in its chemistry. While HCN has been frequently used as a dense gas tracer due to its high critical density (Y. Gao & P. M. Solomon 2004; Y. L. Shirley 2015), some studies have found that the lower- J HCN transitions may actually trace more diffuse gas ($n \lesssim 10^4 \text{ cm}^{-3}$ G. H. Jones et al. 2023). Additionally, several recent studies have suggested that the HCN abundance can be influenced by star-formation feedback mechanisms such as UV (M. G. Santa-Maria et al. 2023) and cosmic-ray (E. Behrens et al. 2022, 2024) ionization. While HCN is largely formed at low CRIR via neutral-neutral reactions with temperature barriers of at least 50 K, higher CRIRs cause HCN to form via recombination reactions involving cosmic-ray electrons, resulting in feedback-dependent formation paths (E. Behrens et al. 2022). Due to these additional factors, HCN's role as a dense gas tracer may not be as straightforward. While HNC is also known as a dense gas tracer (S. Aalto et al. 2002; C. Eibensteiner et al. 2022; M. Imanishi et al. 2023), it may not be affected as strongly by feedback mechanisms. The routes to form HNC at low CRIRs are far less temperature-dependent than those that form HCN (E. Behrens et al. 2022), suggesting that HNC will be

less affected by feedback mechanisms. Assuming that the reaction networks in our chemical model (derived from the UMIST12 database, D. McElroy et al. 2013) are complete, our results indicate that HNC is a more reliable tracer of the gas density than HCN.

5.4. *Sampling the Energy Ladder*

Our results indicate that constraining chemical and radiative transfer models with molecular transitions that span a range of upper-state energies E_u generally improves the constraints as compared to only using either low- or high-energy transitions. The HCN and HNC transitions range in E_u from $\sim 4 - 43$ K (Table 1; R. J. Saykally et al. 1976; V. Ahrens et al. 2002). When constraining gas volume density, CRIR, and the beam-filling factor, Figures 8, 9, and 10 indicate that a combination of the $J = 1 - 0$ HCN and HNC transitions with either or both of the $J = 3 - 2$ and $J = 4 - 3$ transitions are very effective and, in the majority of cases, constrain the median value of these gas parameters within a factor of two. As discussed in Section 4.2, regions with lower gas densities (relative to the high gas densities of $\sim 10^5 \text{ cm}^{-3}$ that we see in the NGC 253 starburst nucleus) may be more easily characterized with the $J = 3 - 2$ versus the $J = 4 - 3$ transitions due to their critical densities. Because critical densities assume a fully optically thin environment, which is likely not the case for HCN and HNC in NGC 253, we will adopt the nomenclature used in Y. L. Shirley (2015) and instead refer to the effective excitation density n_{eff} , which takes into account radiative trapping. n_{eff} is dependent on the gas temperature, and though we cannot constrain kinetic temperature with HCN and HNC, other studies suggest that the temperature is $\sim 80 - 100$ K at distances greater than ~ 100 pc from the center of the CMZ and up to 200 K at the nucleus (J. G. Mangum et al. 2019; K. Tanaka et al. 2024). Under these conditions, the maximum n_{eff} for HCN $J = 1 - 0$, $2 - 1$, $3 - 2$, and $4 - 3$ would be 2.6×10^3 , 7.3×10^3 , 2.5×10^4 , and $8.1 \times 10^4 \text{ cm}^{-3}$, respectively, with similar n_{eff} for HNC (Y. L. Shirley 2015).

Given that the n_{H_2} control median for the low- n - ζ region is $\sim 10^4 \text{ cm}^{-3}$, it is not surprising that using the $J = 3 - 2$ HCN and HNC transitions instead of the $J = 4 - 3$ provides more information on the gas density in this region. Similarly, the $J = 4 - 3$ transitions are more useful in the high- n - ζ region due to its higher median density of $\sim 10^5 \text{ cm}^{-3}$. However, it is important to note that these transitions by themselves may not be very useful for determining the density. Though single transitions appear to constrain the gas density within, at times, a factor of 2 or 3 from the control median in Figures 8, 9, and 10, the uncertainty on these estimates is often large, 4–10 times the control uncertainty. With such a large uncertainty range, the density remains essentially unconstrained. Supplementary corner plots in the Appendix (Figure 2) also show that the posterior distributions for gas density when constrained with sin-

gle transitions often peak at one end of our prior distribution range, which casts some doubt on the validity of these constraints.

Single transitions may not be the most effective to characterize gas parameters because the intensity balance of low- and high- E_u transitions is important and informs the models how each energy level is populated relative to other levels, which can be reflective of the gas density. Additionally, the gas we study is not a single homogeneous structure. Though we derive a single value for the gas density in a given region, this number is simply an average over what is likely several gas components. Lower- E_u transitions may trace a more diffuse gas component, possibly being emitted from a larger area, whereas the higher- E_u transitions are associated with smaller, denser components. In extragalactic astrochemistry, where even the highest resolution measurements are averaging over several gas components, it is critical to obtain measurements of multiple transitions that span the J -ladder in order to fully characterize the gas.

We find that the gas we are probing has an important contribution from the $J = 1 - 0$ transitions. As mentioned in Section 4.2, matched pairs of HCN and HNC transitions that do not include the HCN or HNC $1 - 0$ transitions perform quite poorly. Figures 8, 9, and 10 show that matched transition combinations without the $1 - 0$ almost exclusively fall in the bottom half of the tested combinations. For example, the matched case (X) that includes the HCN and HNC $2 - 1$, $3 - 2$, and $4 - 3$ transitions is one of the worst tested combinations for volume density and CRIR, despite containing six transitions. We find that models that are not constrained by the $1 - 0$ transitions often severely underestimate the $1 - 0$ emission. In this case, the model estimates the HCN $1 - 0$ integrated intensity to be 190 K km s^{-1} , while the measured value is $285 \pm 43 \text{ K km s}^{-1}$. This underestimation clearly impacts the inferred parameter results, causing the algorithm to infer higher volume densities and CRIRs than it would otherwise. In the regions studied here, the HCN and HNC $J = 1 - 0$ transitions clearly contribute significantly to the overall gas emission.

6. CONCLUSION

We examine the efficacy of various combinations of HCN and HNC transitions in constraining kinetic temperature, H_2 volume density, cosmic-ray ionization rate (CRIR), H_2 column density, and a beam-filling factor in three representative 50-pc regions in the NGC 253 CMZ. We calculate residuals of the the posterior distributions for all the test combinations of HCN and HNC transitions as compared to controls, or the posterior distributions obtained when using the $J = 1 - 0$, $2 - 1$, $3 - 2$, and $4 - 3$ transitions of both HCN and HNC. Our conclusions are as follows.

- Single transitions are not effective at constraining gas parameters and generally fall into the worst quartile of combinations we study here. While they may yield volume median densities within a factor of 2-5 of the control, uncertainties on these estimates can be larger by a factor of 5-10.
- Using single transitions or a single molecule (HCN or HNC) to constrain the CRIR results in median CRIRs different from the control by up to an order of magnitude. Single-transition or single-molecule constraints also result in CRIR uncertainties that are 10-50 times greater than that of our control models.
- Including multiple transitions that span a range of upper-state energies is important when inferring gas parameters, especially volume density and CRIR. The intensity balance of these transitions provides constraints for the models, especially when measurements average over a large area that likely contains multiple gas components. In particular, combinations that include the $J = 1 - 0$ transitions and either the $J = 3 - 2$ or $J = 4 - 3$ transitions usually constrain the gas parameters within a factor of 2 of the control medians.
- Most transition combinations yield molecular hydrogen column densities within a factor of two of the control median, with uncertainties 1-6 times that of the control.
- For the beam-filling factor, most models derive median values within a factor of 2-3 of the control median. Uncertainties on the beam-filling factor derivations are generally less than 3 times the control model uncertainty, but can be as large as 7 times the control uncertainty for single or matched HCN and HNC transition models.
- In the case of HCN and HNC, transitions from both species with a range of upper-state energies are required to constrain the CRIR. Using a single species or transitions from multiple species with a limited range in upper-state energies results in poor constraints on the CRIR, with the median CRIR different from the control by up to an order of magnitude.
- HNC is a more direct tracer of gas density than HCN, as HCN emission can be influenced by factors besides volume density (e.g. UV and cosmic-ray ionization). On the other hand, gas density is the main factor contributing to HNC abundances.
- We recommend that the quality metrics provided in Figures 8, 9, and 10 be used by observers to design experiments which provide physical parameter constraints commensurate with the specific needs of their research projects.

These results show that in starburst environments that feature complex chemistry as a result of competing star-formation feedback mechanisms, multiple transitions of multiple molecular species are required in order to accurately and precisely constrain the conditions of dense gas. More work is needed to understand how these results might extend to non-starburst environments or those dominated by different chemical and feedback mechanisms, such as shocked or photodissociation regions.

ACKNOWLEDGMENTS

The authors thank R. Indebetouw for encouraging the pursuit of this project. The authors also thank K. D. Foster for productive conversations that have improved the quality of this work. This paper makes use of the following ALMA data: ADS/JAO.ALMA #2017.1.00161.L and 2018.1.00162.S. ALMA is a partnership of ESO (representing its member states), NSF (USA) and NINS (Japan), together with NRC (Canada), MOST and ASIAA (Taiwan), and KASI (Republic of Korea), in cooperation with the Republic of Chile. The Joint ALMA Observatory is operated by ESO, AUI/NRAO and NAOJ. The National Radio As-

tronomy Observatory and Green Bank Observatory are facilities of the U.S. National Science Foundation operated under cooperative agreement by Associated Universities, Inc. Support for this work was provided by the NSF through the Grote Reber Fellowship Program administered by Associated Universities, Inc./National Radio Astronomy Observatory.

AUTHOR CONTRIBUTIONS

EB led the development of the modeling, analysis, interpretation of the results, development of effective presentation of those results, and writing of the article. JGM provided guidance regarding the interpretation of the results and overall project direction. MB, CE, and SV contributed to the interpretation and presentation of the results. SV provided guidance regarding the astrochemistry presented in this article.

Facility: ALMA

Software: `Astropy` ([Astropy Collaboration et al. 2013, 2018, 2022](#)), `CASA` ([CASA Team et al. 2022](#)), `corner` ([D. Foreman-Mackey 2016](#)), `Nautilus` ([J. U. Lange 2023](#)), `SpectralRadex`⁷, `TensorFlow` ([M. Abadi et al. 2015](#)), `UCLCHEM` ([J. Holdship et al. 2017](#)).

REFERENCES

Aalto, S., Polatidis, A. G., Hüttemeister, S., & Curran, S. J. 2002, *A&A*, 381, 783, doi: [10.1051/0004-6361:20011514](https://doi.org/10.1051/0004-6361:20011514)

Abadi, M., Agarwal, A., Barham, P., et al. 2015, <https://www.tensorflow.org/>

Agertz, O., Kravtsov, A. V., Leitner, S. N., & Gnedin, N. Y. 2013, *ApJ*, 770, 25, doi: [10.1088/0004-637X/770/1/25](https://doi.org/10.1088/0004-637X/770/1/25)

Ahrens, V., Lewen, F., Takano, S., et al. 2002, *Zeitschrift Naturforschung Teil A*, 57, 669, doi: [10.1515/zna-2002-0806](https://doi.org/10.1515/zna-2002-0806)

Astropy Collaboration, Robitaille, T. P., Tollerud, E. J., et al. 2013, *A&A*, 558, A33, doi: [10.1051/0004-6361/201322068](https://doi.org/10.1051/0004-6361/201322068)

Astropy Collaboration, Price-Whelan, A. M., Sipőcz, B. M., et al. 2018, *AJ*, 156, 123, doi: [10.3847/1538-3881/aabc4f](https://doi.org/10.3847/1538-3881/aabc4f)

Astropy Collaboration, Price-Whelan, A. M., Lim, P. L., et al. 2022, *ApJ*, 935, 167, doi: [10.3847/1538-4357/ac7c74](https://doi.org/10.3847/1538-4357/ac7c74)

Bao, M., Harada, N., Kohno, K., et al. 2024, *A&A*, 687, A43, doi: [10.1051/0004-6361/202349050](https://doi.org/10.1051/0004-6361/202349050)

Behrens, E., Mangum, J. G., Holdship, J., et al. 2022, *ApJ*, 939, 119, doi: [10.3847/1538-4357/ac91ce](https://doi.org/10.3847/1538-4357/ac91ce)

Behrens, E., Mangum, J. G., Viti, S., et al. 2024, arXiv, arXiv:2409.13821, doi: [10.48550/arXiv.2409.13821](https://doi.org/10.48550/arXiv.2409.13821)

Bemis, A. R., Wilson, C. D., Sharda, P., Roberts, I. D., & He, H. 2024, *A&A*, 692, A146, doi: [10.1051/0004-6361/202347879](https://doi.org/10.1051/0004-6361/202347879)

Bouvier, M., Viti, S., Behrens, E., et al. 2024, arXiv, arXiv:2405.08408, doi: [10.48550/arXiv.2405.08408](https://doi.org/10.48550/arXiv.2405.08408)

Bouvier, M., Viti, S., Mangum, J. G., et al. 2025, arXiv, arXiv:2504.19631, doi: [10.48550/arXiv.2504.19631](https://doi.org/10.48550/arXiv.2504.19631)

Butterworth, J., Viti, S., Van der Werf, P. P., et al. 2024, arXiv, arXiv:2402.10721, doi: [10.48550/arXiv.2402.10721](https://doi.org/10.48550/arXiv.2402.10721)

CASA Team, Bean, B., Bhatnagar, S., et al. 2022, *PASP*, 134, 114501, doi: [10.1088/1538-3873/ac9642](https://doi.org/10.1088/1538-3873/ac9642)

Ceverino, D., & Klypin, A. 2009, *ApJ*, 695, 292, doi: [10.1088/0004-637X/695/1/292](https://doi.org/10.1088/0004-637X/695/1/292)

Eibensteiner, C., Barnes, A. T., Bigiel, F., et al. 2022, *A&A*, 659, A173, doi: [10.1051/0004-6361/202142624](https://doi.org/10.1051/0004-6361/202142624)

Feroz, F., Hobson, M. P., Cameron, E., & Pettitt, A. N. 2019, *The Open Journal of Astrophysics*, 2, 10, doi: [10.21105/astro.1306.2144](https://doi.org/10.21105/astro.1306.2144)

Foreman-Mackey, D. 2016, *The Journal of Open Source Software*, 1, 24, doi: [10.21105/joss.00024](https://doi.org/10.21105/joss.00024)

Gao, Y., & Solomon, P. M. 2004, *ApJ*, 606, 271, doi: [10.1086/382999](https://doi.org/10.1086/382999)

García-Burillo, S., Usero, A., Alonso-Herrero, A., et al. 2012, *A&A*, 539, A8, doi: [10.1051/0004-6361/201117838](https://doi.org/10.1051/0004-6361/201117838)

⁷ <https://spectralradex.readthedocs.io/en/latest/>

García-Rodríguez, A., Usero, A., Leroy, A. K., et al. 2023, *A&A*, 672, A96, doi: [10.1051/0004-6361/202244317](https://doi.org/10.1051/0004-6361/202244317)

Gong, Y., Henkel, C., Bop, C. T., et al. 2025, arXiv, arXiv:2502.20894, doi: [10.48550/arXiv.2502.20894](https://doi.org/10.48550/arXiv.2502.20894)

Haasler, D., Rivilla, V. M., Martín, S., et al. 2022, *A&A*, 659, A158, doi: [10.1051/0004-6361/202142032](https://doi.org/10.1051/0004-6361/202142032)

Hacar, A., Bosman, A. D., & van Dishoeck, E. F. 2020, *A&A*, 635, A4, doi: [10.1051/0004-6361/201936516](https://doi.org/10.1051/0004-6361/201936516)

Harada, N., Martín, S., Mangum, J. G., et al. 2021, *ApJ*, 923, 24, doi: [10.3847/1538-4357/ac26b8](https://doi.org/10.3847/1538-4357/ac26b8)

Harada, N., Martín, S., Mangum, J. G., et al. 2022, *ApJ*, 938, 80, doi: [10.3847/1538-4357/ac8dfc](https://doi.org/10.3847/1538-4357/ac8dfc)

Harada, N., Meier, D. S., Martín, S., et al. 2024, *ApJS*, 271, 38, doi: [10.3847/1538-4365/ad1937](https://doi.org/10.3847/1538-4365/ad1937)

Heckman, T. M., Armus, L., & Miley, G. K. 1990, *ApJS*, 74, 833, doi: [10.1086/191522](https://doi.org/10.1086/191522)

Hernández-Vera, C., Guzmán, V. V., Goicoechea, J. R., et al. 2023, *A&A*, 677, A152, doi: [10.1051/0004-6361/202347206](https://doi.org/10.1051/0004-6361/202347206)

Holdship, J., Viti, S., Jiménez-Serra, I., Makrymallis, A., & Priestley, F. 2017, *AJ*, 154, 38, doi: [10.3847/1538-3881/aa773f](https://doi.org/10.3847/1538-3881/aa773f)

Holdship, J., Viti, S., Martín, S., et al. 2021, *A&A*, 654, A55, doi: [10.1051/0004-6361/202141233](https://doi.org/10.1051/0004-6361/202141233)

Holdship, J., Mangum, J. G., Viti, S., et al. 2022, *ApJ*, 931, 89, doi: [10.3847/1538-4357/ac6753](https://doi.org/10.3847/1538-4357/ac6753)

Hopkins, P. F., Quataert, E., & Murray, N. 2012, *MNRAS*, 421, 3522, doi: [10.1111/j.1365-2966.2012.20593.x](https://doi.org/10.1111/j.1365-2966.2012.20593.x)

Huang, K. Y., Viti, S., Holdship, J., et al. 2023, *A&A*, 675, A151, doi: [10.1051/0004-6361/202245659](https://doi.org/10.1051/0004-6361/202245659)

Humire, P. K., Henkel, C., Hernández-Gómez, A., et al. 2022, *A&A*, 663, A33, doi: [10.1051/0004-6361/202243384](https://doi.org/10.1051/0004-6361/202243384)

Imanishi, M., Baba, S., Nakanishi, K., & Izumi, T. 2023, *ApJ*, 950, 75, doi: [10.3847/1538-4357/acc388](https://doi.org/10.3847/1538-4357/acc388)

Jones, G. H., Clark, P. C., Glover, S. C. O., & Hacar, A. 2023, *MNRAS*, 520, 1005, doi: [10.1093/mnras/stad202](https://doi.org/10.1093/mnras/stad202)

Kishikawa, R., Harada, N., Saito, T., et al. 2024, *Publications of the Astronomical Society of Japan*, 77, 1, doi: [10.1093/pasj/pssae095](https://doi.org/10.1093/pasj/pssae095)

Lange, J. U. 2023, *Monthly Notices of the Royal Astronomical Society*, 525, 3181, doi: [10.1093/mnras/stad2441](https://doi.org/10.1093/mnras/stad2441)

Lehnert, M. D., & Heckman, T. M. 1996, *ApJ*, 462, 651, doi: [10.1086/177180](https://doi.org/10.1086/177180)

Leroy, A. K., Bolatto, A. D., Ostriker, E. C., et al. 2015, *ApJ*, 801, 25, doi: [10.1088/0004-637X/801/1/25](https://doi.org/10.1088/0004-637X/801/1/25)

Li, F., Wang, J., Fang, M., et al. 2020, *PASJ*, 72, 41, doi: [10.1093/pasj/pssaa025](https://doi.org/10.1093/pasj/pssaa025)

Mangum, J. G., Ginsburg, A. G., Henkel, C., et al. 2019, *ApJ*, 871, 170, doi: [10.3847/1538-4357/aafa15](https://doi.org/10.3847/1538-4357/aafa15)

Martín, S., Mangum, J. G., Harada, N., et al. 2021, *A&A*, 656, A46, doi: [10.1051/0004-6361/202141567](https://doi.org/10.1051/0004-6361/202141567)

McElroy, D., Walsh, C., Markwick, A. J., et al. 2013, *A&A*, 550, A36, doi: [10.1051/0004-6361/201220465](https://doi.org/10.1051/0004-6361/201220465)

Neumann, L., Bigiel, F., Barnes, A. T., et al. 2024, *A&A*, 691, A121, doi: [10.1051/0004-6361/202449496](https://doi.org/10.1051/0004-6361/202449496)

Onus, A., Krumholz, M. R., & Federrath, C. 2018, *MNRAS*, 479, 1702, doi: [10.1093/mnras/sty1662](https://doi.org/10.1093/mnras/sty1662)

Oteo, I., Zhang, Z. Y., Yang, C., et al. 2017, *ApJ*, 850, 170, doi: [10.3847/1538-4357/aa8ee3](https://doi.org/10.3847/1538-4357/aa8ee3)

Patra, S., Evans, N. J., Kim, K.-T., et al. 2025, *ApJ*, 983, 133, doi: [10.3847/1538-4357/adbf8d](https://doi.org/10.3847/1538-4357/adbf8d)

Peschken, N., Hanasz, M., Naab, T., Wóltański, D., & Gawryszczak, A. 2023, *MNRAS*, 522, 5529, doi: [10.1093/mnras/stad1358](https://doi.org/10.1093/mnras/stad1358)

Reach, W. T., Tram, L. N., Richter, M., Gusdorf, A., & DeWitt, C. 2019, *ApJ*, 884, 81, doi: [10.3847/1538-4357/ab41f7](https://doi.org/10.3847/1538-4357/ab41f7)

Rekola, R., Richer, M. G., McCall, M. L., et al. 2005, *MNRAS*, 361, 330, doi: [10.1111/j.1365-2966.2005.09166.x](https://doi.org/10.1111/j.1365-2966.2005.09166.x)

Rybak, M., Hodge, J. A., Greve, T. R., et al. 2022, *A&A*, 667, A70, doi: [10.1051/0004-6361/202243894](https://doi.org/10.1051/0004-6361/202243894)

Santa-Maria, M. G., Goicoechea, J. R., Pety, J., et al. 2023, *A&A*, 679, A4, doi: [10.1051/0004-6361/202346598](https://doi.org/10.1051/0004-6361/202346598)

Saykally, R. J., Szanto, P. G., Anderson, T. G., & Woods, R. C. 1976, *ApJL*, 204, L143, doi: [10.1086/182074](https://doi.org/10.1086/182074)

Schinnerer, E., & Leroy, A. K. 2024, *ARA&A*, 62, 369, doi: [10.1146/annurev-astro-071221-052651](https://doi.org/10.1146/annurev-astro-071221-052651)

Shirley, Y. L. 2015, *PASP*, 127, 299, doi: [10.1086/680342](https://doi.org/10.1086/680342)

Spilker, J. S., Marrone, D. P., Aguirre, J. E., et al. 2014, *ApJ*, 785, 149, doi: [10.1088/0004-637X/785/2/149](https://doi.org/10.1088/0004-637X/785/2/149)

Tanaka, K., Mangum, J. G., Viti, S., et al. 2024, *ApJ*, 961, 18, doi: [10.3847/1538-4357/ad0e64](https://doi.org/10.3847/1538-4357/ad0e64)

Tu, T.-Y., Chen, Y., & Liu, Q.-C. 2025, *ApJ*, 978, 83, doi: [10.3847/1538-4357/ad9390](https://doi.org/10.3847/1538-4357/ad9390)

Turner, J. L., & Ho, P. T. P. 1985, *ApJL*, 299, L77, doi: [10.1086/184584](https://doi.org/10.1086/184584)

Usero, A., Leroy, A. K., Walter, F., et al. 2015, *AJ*, 150, 115, doi: [10.1088/0004-6256/150/4/115](https://doi.org/10.1088/0004-6256/150/4/115)

van der Tak, F. F. S., Black, J. H., Schöier, F. L., Jansen, D. J., & van Dishoeck, E. F. 2007, *A&A*, 468, 627, doi: [10.1051/0004-6361:20066820](https://doi.org/10.1051/0004-6361:20066820)

Vaupré, S., Hily-Blant, P., Ceccarelli, C., et al. 2014, *A&A*, 568, A50, doi: [10.1051/0004-6361/201424036](https://doi.org/10.1051/0004-6361/201424036)

Xu, J.-L., Zavagno, A., Yu, N., et al. 2019, *A&A*, 627, A27, doi: [10.1051/0004-6361/201935024](https://doi.org/10.1051/0004-6361/201935024)

APPENDIX

A. ADDITIONAL FIGURES

In the following, we present additional figures to supplement those in the main text. In Figure 1, we show the full corner plots for our models constrained by the control combinations of HCN and HNC transitions (the $J = 1 - 0$, $2 - 1$, $3 - 2$, and $4 - 3$ for both molecules) for the low- $n\zeta$ and low-SNR regions, as the control result for the high- $n\zeta$ region is shown in Figure 2.

To show examples of what the full 1- and 2-D posterior distributions for models constrained by each of the five transition test combinations may look like, we provide two corner plots for each of the five combination groupings. Though not every transition combination within a particular group will yield similar results, we show examples that are roughly representative of the constraining combinations in each group. The posterior distributions obtained from single transitions (♦) are shown in Figure 2, matched HCN and HNC transitions (✗) are shown in Figure 3, single molecule combinations (■) are shown in Figure 4, all transitions of one molecule supplemented with one transition from the other (●) are shown in Figure 5, and single transitions removed (▲) are shown in Figure 6.

We supplement Figure 2 showing the parameter results from measured versus synthetic data (Section 3.5 with additional figures for test cases constrained by just the HCN $1 - 0$ transition (Figure 7) and just the four HNC transitions (Figure 8).

We also provide versions of Figure 7 for the high- $n\zeta$ region (Figure 9) and for the the low-SNR region (Figure 10).

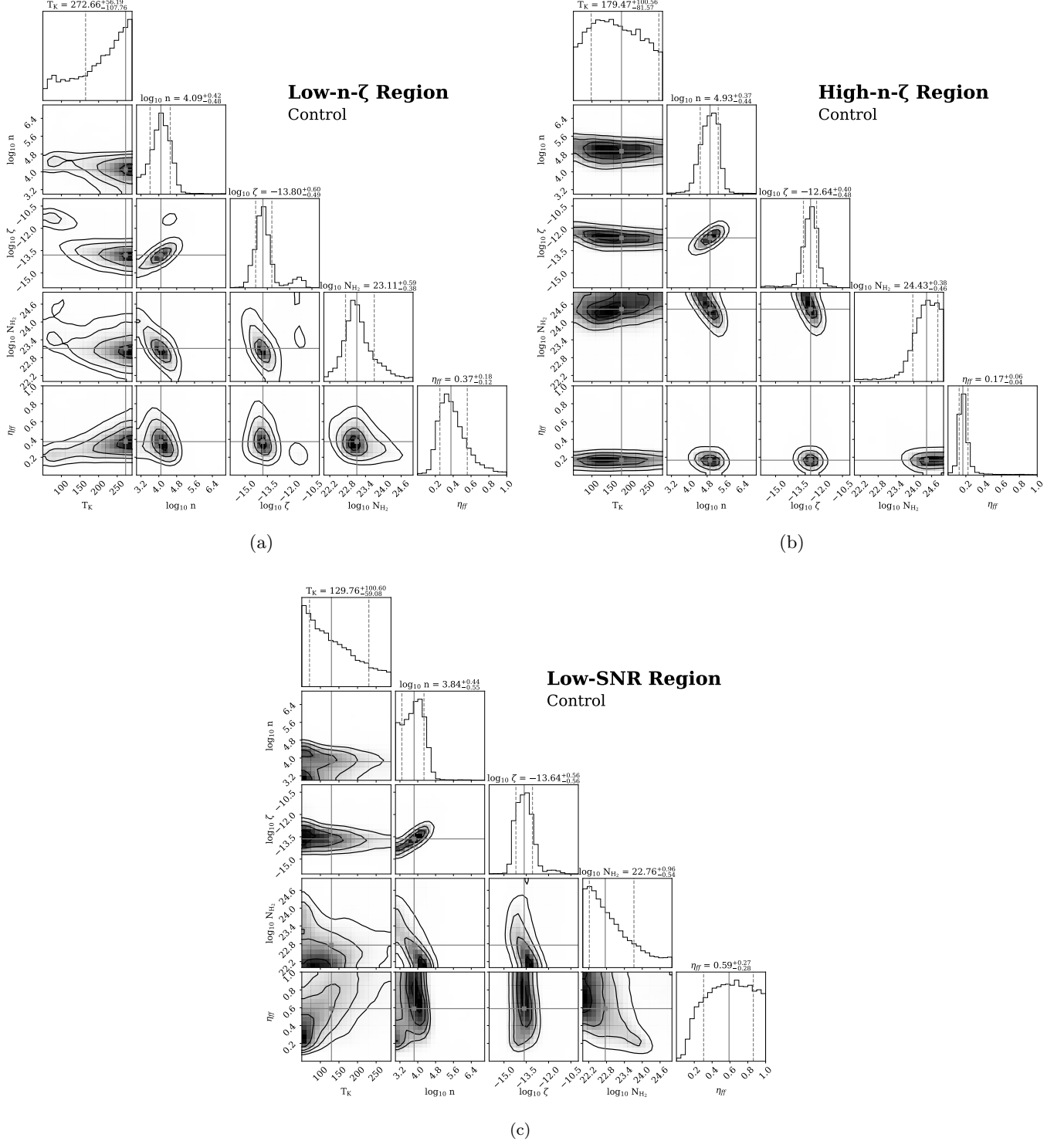


Figure 1. Posterior distributions for the low- n - ζ region (top left), high- n - ζ region (top right), and low-SNR region (bottom) using the control set of HCN and HNC transitions.

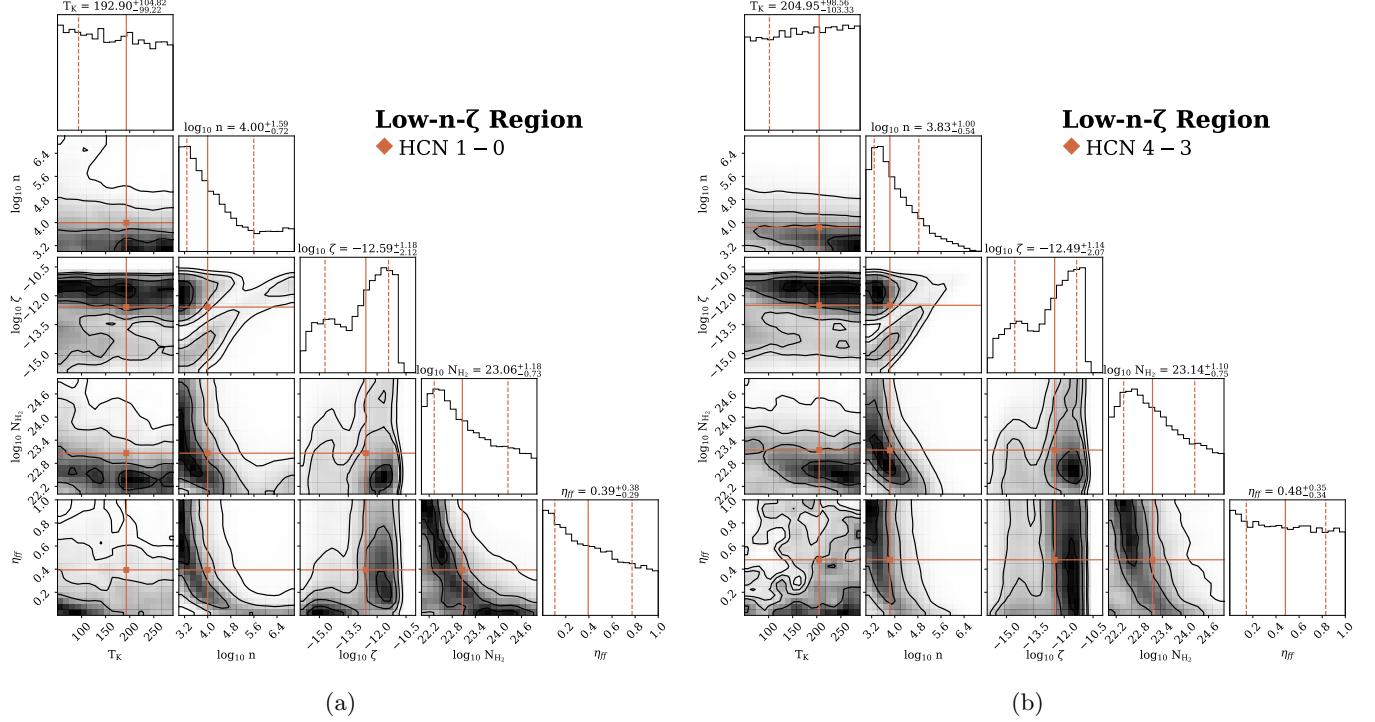


Figure 2. Corner plots for two examples where we constrain our models with single transitions in the low- n - ζ region: (a) HCN 1 = 0 and (b) HCN 4 – 3.

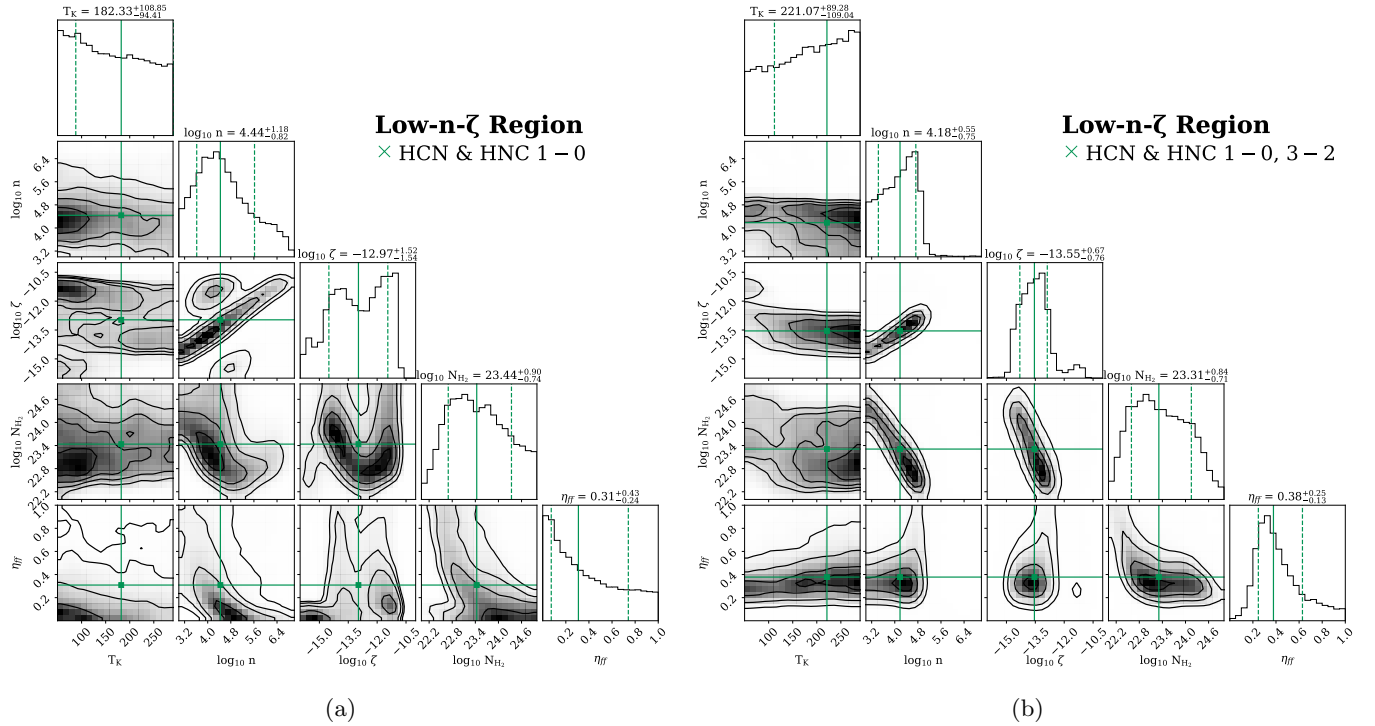


Figure 3. Same as in Figure 2 but for two examples of matched HCN and HNC transitions: (a): HCN and HNC 1 – 0 and (b) HCN and HNC 1 – 0 and 3 – 2.

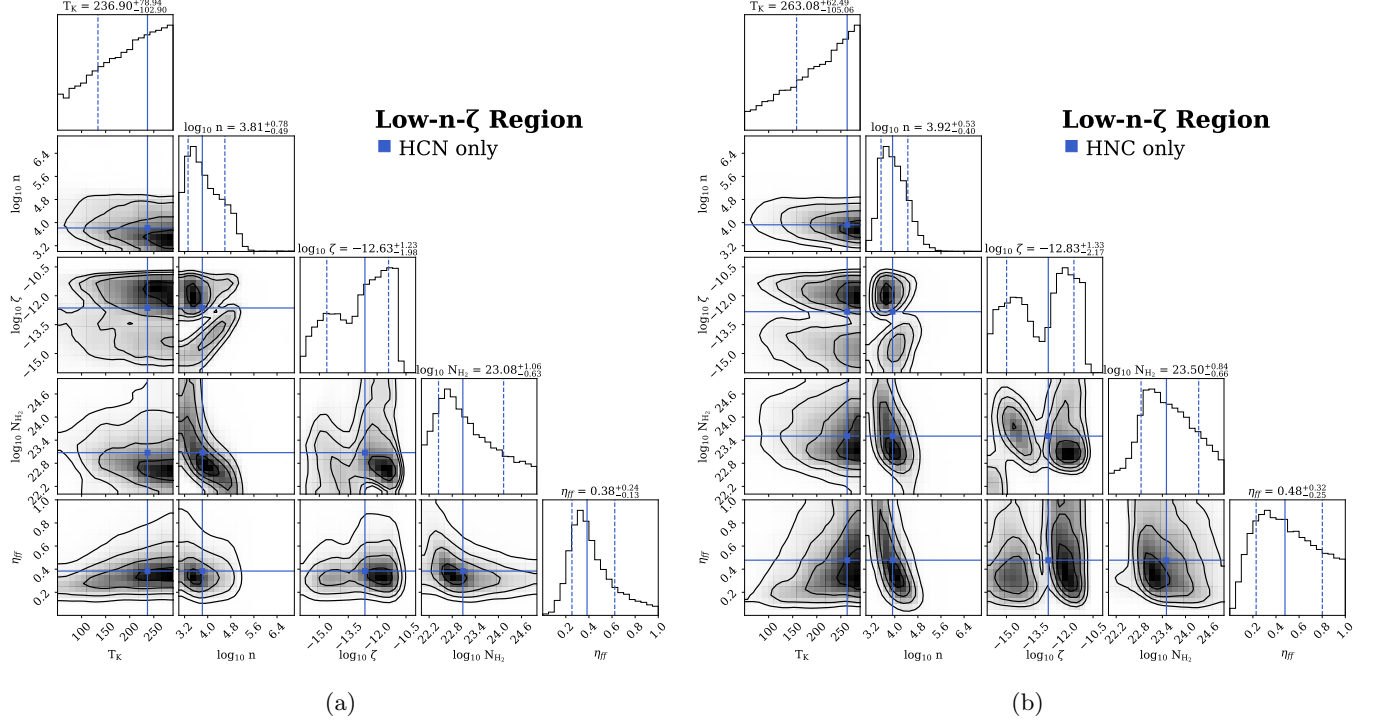


Figure 4. Same as in Figures 2 and 3 but for two examples of combinations where we use all the transitions of a single molecule: (a): HCN only and (b) HNC only.

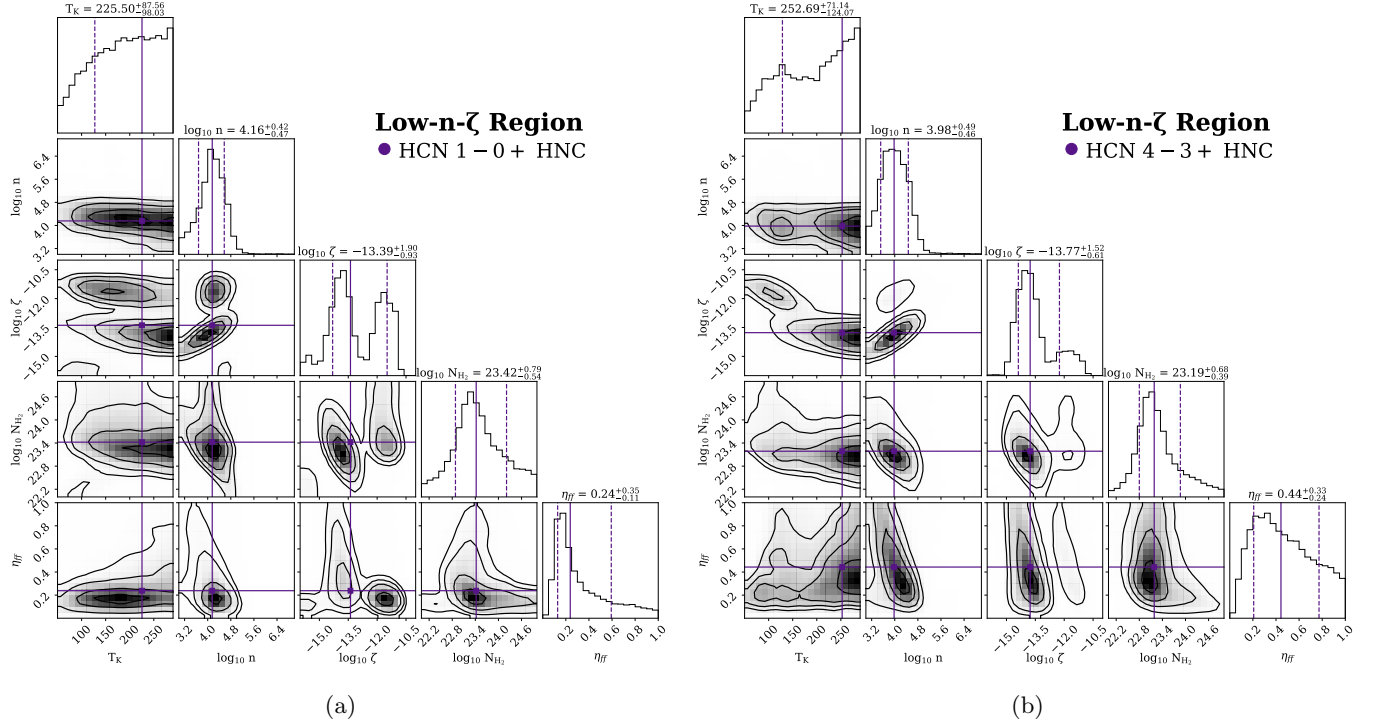


Figure 5. Same as in Figures 2, 3, and 4 but for two examples of combinations where we use all the transitions of one molecule supplemented with a single transition of the opposing molecule: (a): HCN 1 – 0 + all HNC (b) HCN 4 – 3 + all HNC.

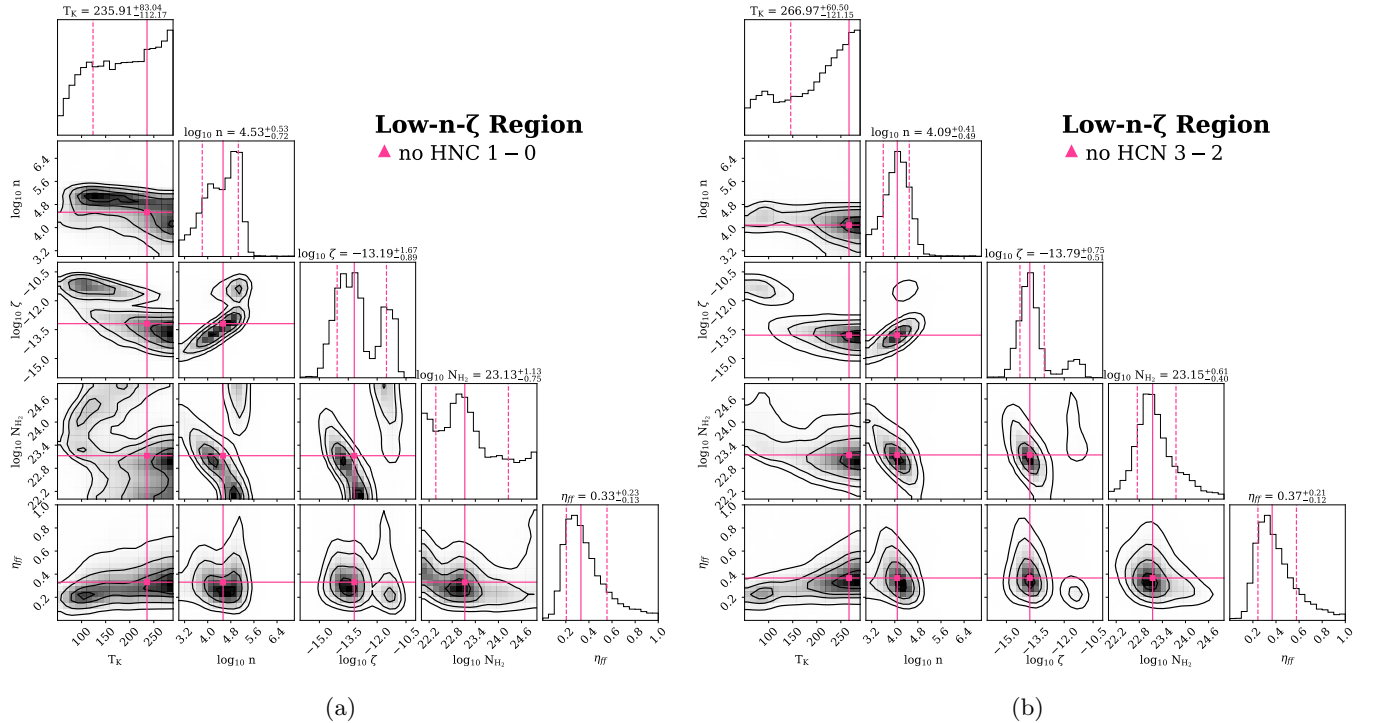


Figure 6. Same as in Figures 2, 3, 4, and 5 but for two examples of combinations where we remove a single transition from the set of 8: (a): no HNC 1 – 0 (b) no HCN 3 – 2.

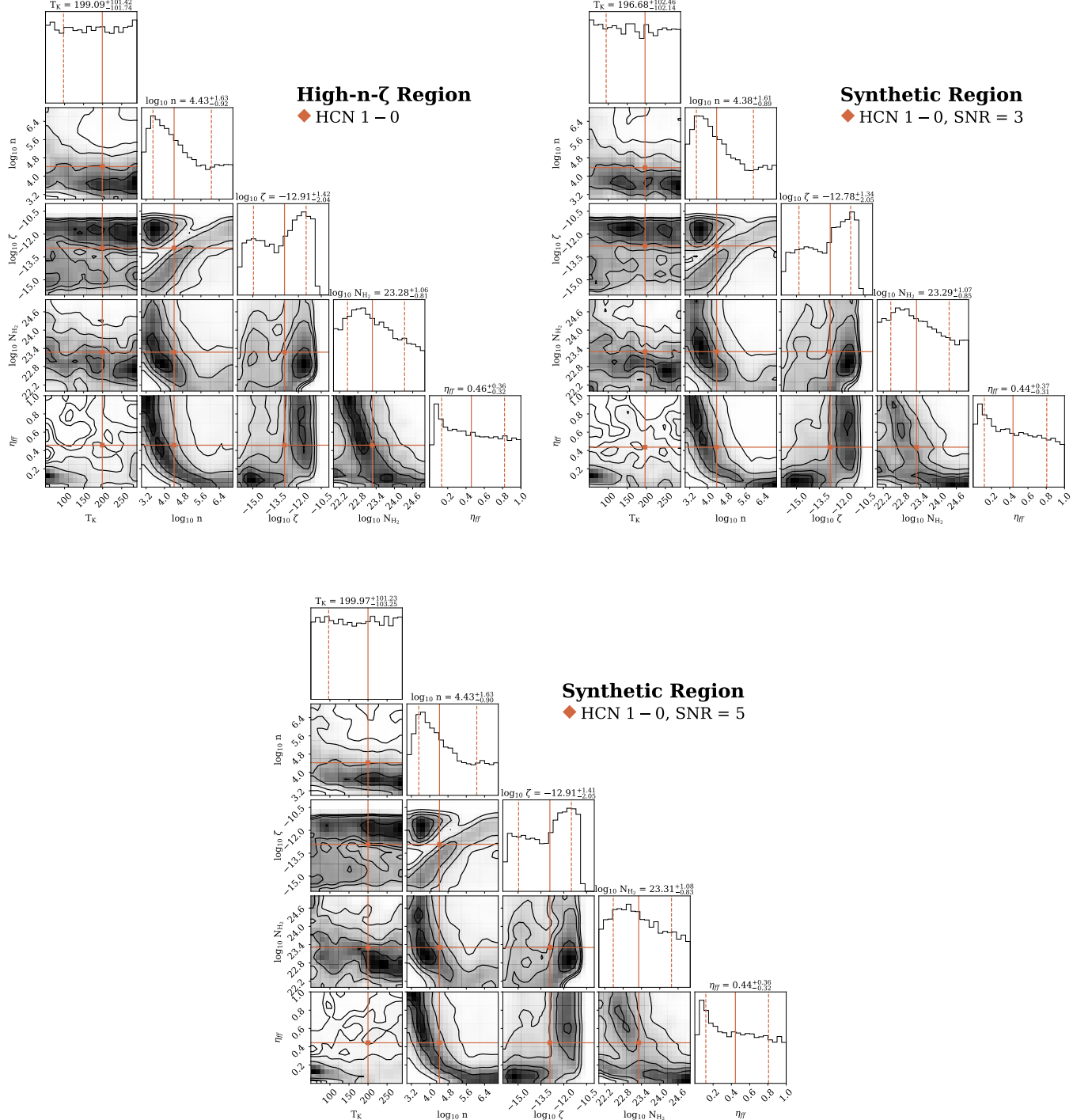


Figure 7. Bayesian inference results for the models constrained solely by HCN 1 – 0 for the high- n - ζ (top left) and synthetic regions with SNR = 3 (top right) and SNR = 5 (bottom).

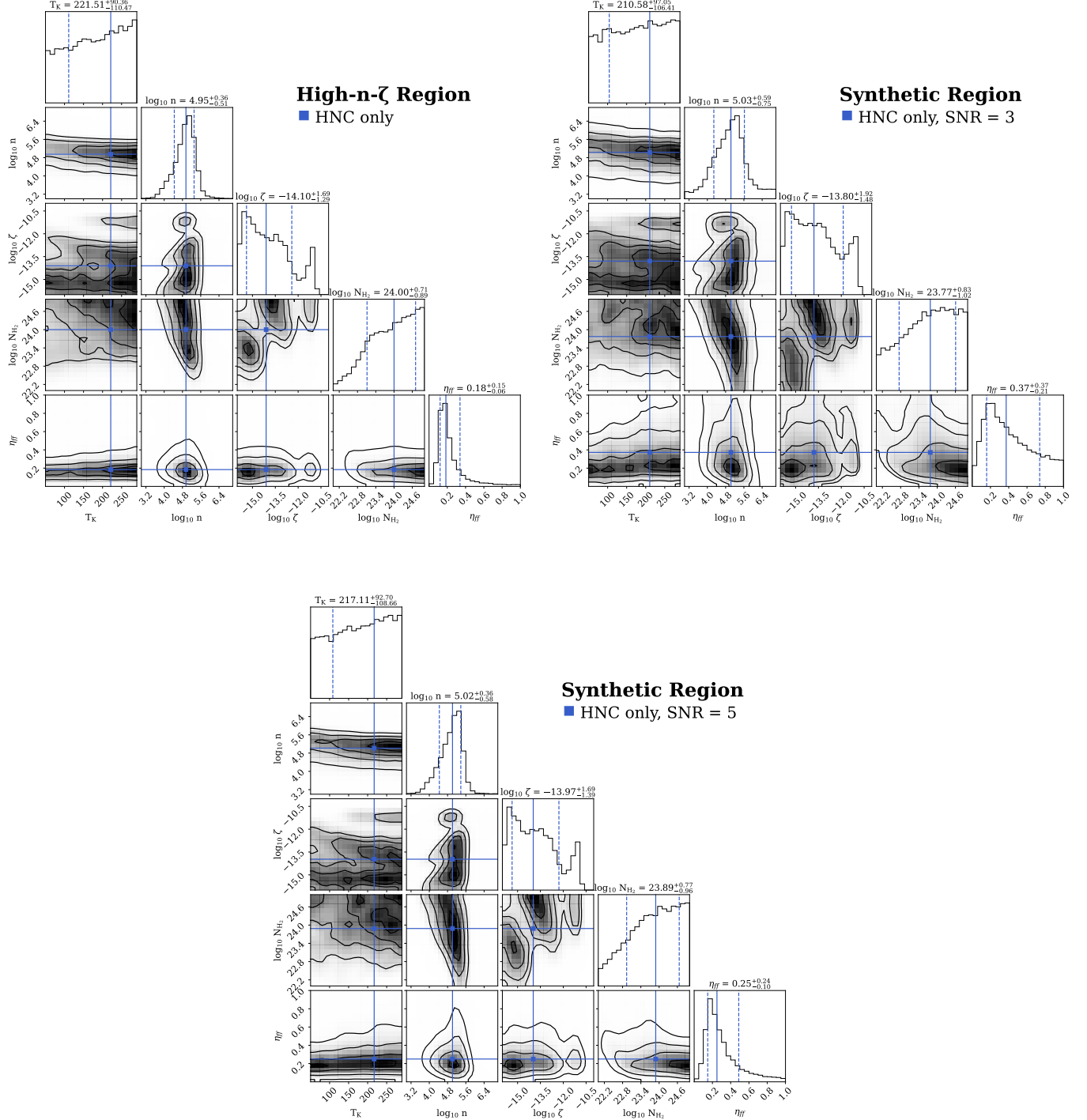


Figure 8. Bayesian inference results for the models constrained solely by HNC transitions for the high- n - ζ (top left) and synthetic regions for SNR = 3 (top right) and SNR = 5 (bottom).

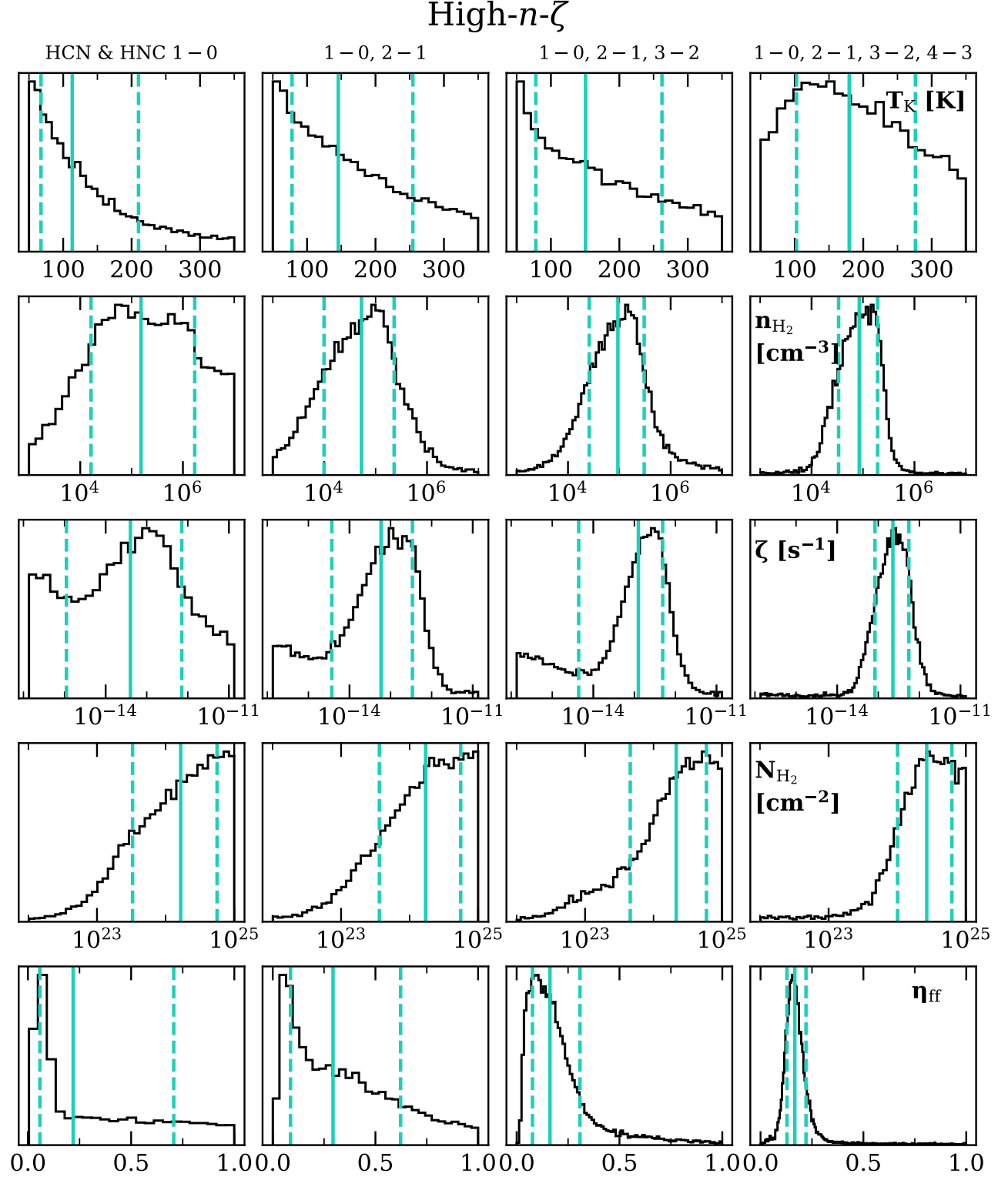


Figure 9. Same as in Figure 7 but for the high- $n\text{-}\zeta$ region.

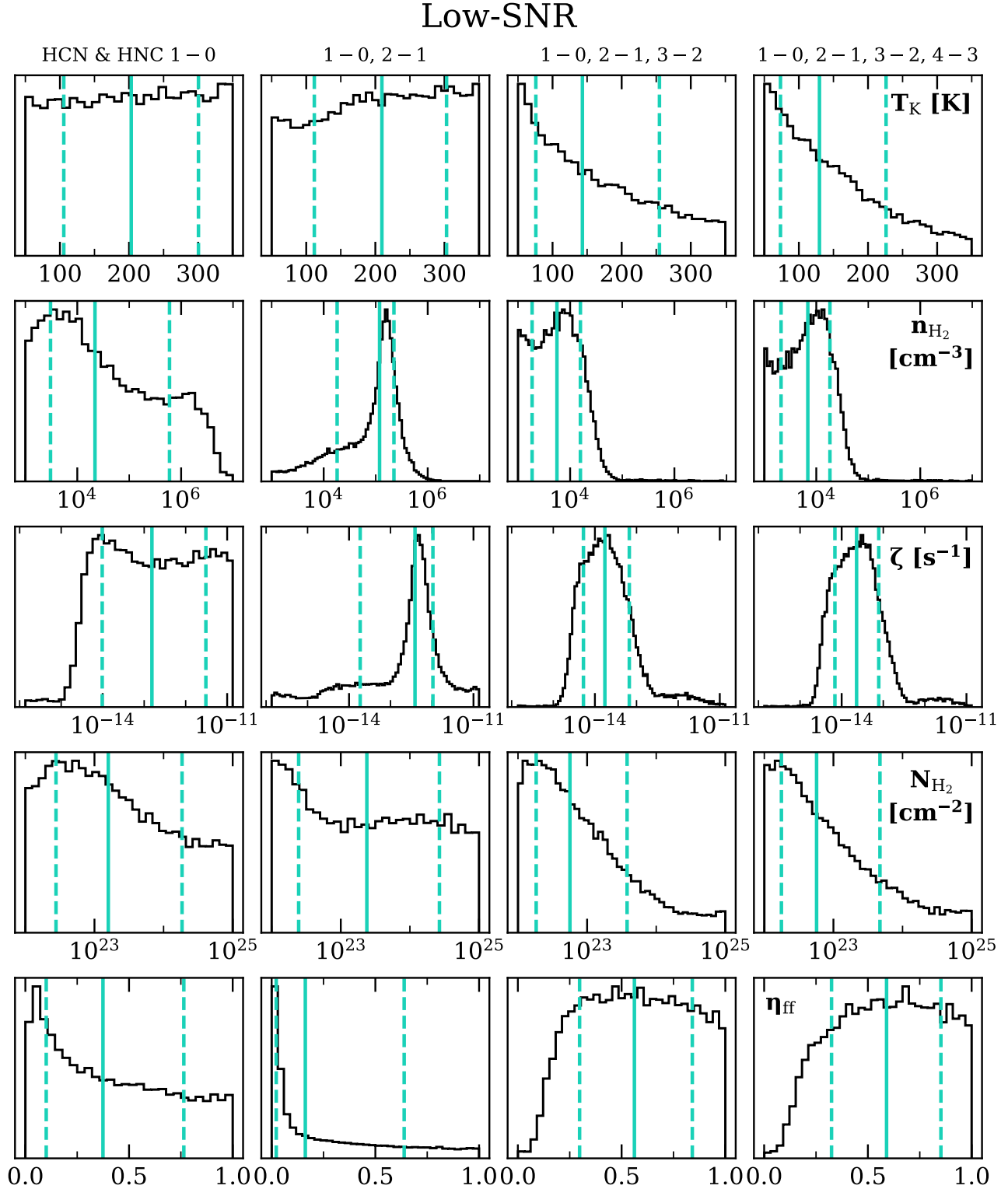


Figure 10. Same as in Figure 7 and 9 but for the low-SNR region.

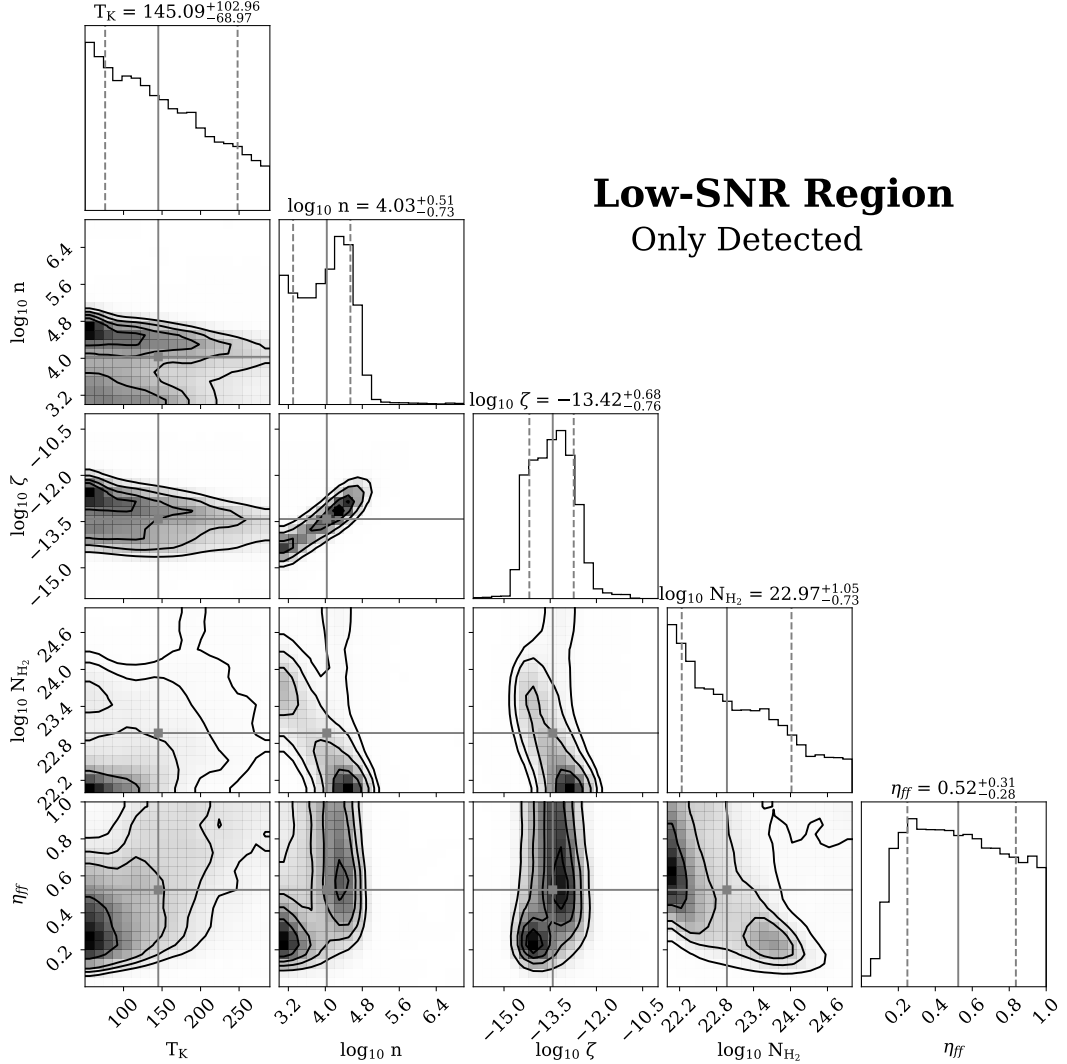


Figure 11. Inference results for low-SNR region where models were constrained with only the 5 detected transitions (no upper limits). These results are very similar to those seen in the low-SNR panel of Figure 1, indicating that the 3σ upper limits do not have a large impact on the parameter inference results.